INTERNATIONAL JOURNAL FOR NUMERICAL METHODS IN ENGINEERING
*Int. J. Numer. Meth. Engng* (2013)
Published online in Wiley Online Library (wileyonlinelibrary.com). DOI: 10.1002/nme.4466

# An augmentation technique for large deformation frictional contact problems

M. Franke, C. Hesch*,† and P. Betsch

*Chair of Computational Mechanics, Department of Mechanical Engineering, University of Siegen, Germany*

SUMMARY

The present work deals with a new approach to frictional large deformation contact problems. In particular, a new formulation of the frictional kinematics is introduced that is based on a specific augmentation technique used for the introduction of additional variables. This augmentation technique substantially simplifies the formulation of the whole system. A size reduction of the resulting system of algebraic equations is proposed. Consequently, the augmentation technique does not lead to an increase in size of the algebraic system of equations to be ultimately solved. The size reduction retains the simplicity of the formulation and preserves important conservation laws such as conservation of angular momentum. Copyright © 2013 John Wiley & Sons, Ltd.

Received 26 July 2012; Revised 26 November 2012; Accepted 3 December 2012

KEY WORDS: frictional contact; Coulomb's law; node-to-surface method; Lagrange multipliers; augmentation

## 1. INTRODUCTION

The development of numerical methods for frictional contact problems is one of the most challenging task in the field of computational sciences. It combines several fields of research, including optimization theory to deal with arising inequality constraints, the development of appropriate discretization schemes in space and time, and tribology for the physical modeling of the surface interaction.

The numerical model to be developed can be subdivided into different tasks, using constitutive laws to describe the physical nature of the surface interaction and, on the other hand, kinematic relations to embed these laws into the generally nonlinear finite element method. We omit any small deformation considerations and focus on the large deformation frictional contact problem. For a comprehensive survey of contemporary methods, we refer to the textbooks of Laursen [1] and Wriggers [2].

Within this paper, we focus on the development of a new method for the contact kinematics. The governing constitutive laws have been extensively investigated by several authors (see among others He and Curnier [3] and Laursen and Oancea [4]). We apply the well-known Coulomb's law, using the established analogy between Coulomb friction and nonassociative plasticity (see for example [5]). However, the proposed approach is capable to embed all kinds of constitutive friction laws.

Our approach follows the lines of the work of Laursen [1, 6], referred to herein as the direct approach [7]. Therefore, in contrast to earlier works (see for example Wriggers and Simo [8] and Parisch [9]), continuum mechanical arguments are used to derive the underlying variational formulation.

*Correspondence to: C. Hesch, Chair of Computational Mechanics, Department of Mechanical Engineering, University of Siegen, Germany.

†E-mail: christian.hesch@uni-siegen.de

In contrast to previous works dealing with large deformation frictional contact, we propose a new augmentation technique for the description of the frictional kinematics. The augmentation technique relies on the introduction of additional variables representing the local convective coordinates. Note that the terminus augmentation is widely used for different methods, including the augmented Lagrangian update algorithm. Within our newly proposed method for frictional contact, we refer to augmentation techniques as used in the context of multibody systems [10]. The additional variables are connected to the original ones by introducing additional algebraic constraints that are enforced by means of Lagrange multipliers. When compared with the traditional direct approach, the augmentation technique significantly simplifies the whole formulation.

After the discretization in space has been performed, the resulting differential-algebraic equations can be reformulated to reduce the size of the algebraic system to be eventually solved. That is, applying a size-reduction procedure within the discrete setting essentially recovers the size of the original system. It is worth noting that the size-reduction process does not affect the algorithmic conservation properties of the proposed discretization in space and time. In particular, our discretization approach inherits the conservation laws for linear and angular momentum from the underlying continuous formulation.

The development of structure-preserving time-stepping schemes for large deformation contact problems has been subject of extensive research, see Laursen and Chawla [11, 12], Armero and Petöcz [13, 14], and Hesch and Betsch [15, 16]. Similar to these works, the spatial discretization of the contact surface used in the present work is based on the node-to-surface (NTS) method. The extension to more sophisticated models using mortar-based formulations [17–22] will be dealt with in a subsequent work.

The article is organized as follows. The fundamental equations of the underlying problem in strong and weak form are outlined in Section 2. In this connection, the well-established description of the frictional kinematics is summarized, and the newly proposed augmentation technique is introduced. The spatial discretization and the NTS method together with the specific formulation of the augmentation technique is given in Section 3. In Section 4, we apply a suitable time integration scheme and verify algorithmic conservation of linear and angular momentum. Representative numerical examples are presented in Section 5. Eventually, conclusions are drawn in Section 6.

## 2. GOVERNING EQUATIONS

We consider continuum bodies $\mathcal{B}_0^{(i)} \subset \mathbb{R}^3, i \in \{1, ..., k\}$ written in their reference configurations for the large deformation problem at hand. To characterize the deformation, we assume the existence of a mapping $\boldsymbol{\varphi}^{(i)} : \mathcal{B}_0^{(i)} \times [0, T] \to \mathbb{R}^3$, $\boldsymbol{\varphi}^{(i)} = \boldsymbol{\varphi}^{(i)}(\boldsymbol{X}^{(i)}, t)$, such that we can introduce the deformation gradient $\boldsymbol{F}^{(i)} : \mathcal{B}_0^{(i)} \times [0, T] \to \mathbb{R}^{3\times3}$ as follows:

$$\boldsymbol{F}^{(i)} = \frac{\partial \boldsymbol{\varphi}^{(i)}}{\partial \boldsymbol{X}^{(i)}} \tag{1}$$

Note that $\boldsymbol{F}^{(i)}$ remains nonsingular and invertible throughout the considered time interval $\mathcal{I} := [0,\ T]$, that is, $J^{(i)} := \det(\boldsymbol{F}^{(i)}) > 0\ \forall t \in \mathcal{I}$. The material behavior is governed by the strain energy function $W(\boldsymbol{C}^{(i)}) : \mathcal{B}_0^{(i)} \times [0, T] \to \mathbb{R}$ where $\boldsymbol{C} : \mathcal{B}_0^{(i)} \times [0, T] \to \mathbb{R}^{3\times3}$, $\boldsymbol{C} = \boldsymbol{F}^T \boldsymbol{F}$ denotes the right Cauchy–Green tensor, and we define the first Piola–Kirchhoff stress tensor as follows:

$$\boldsymbol{P}^{(i)} = \boldsymbol{F}^{(i)}\, \frac{\partial W^{(i)}(\boldsymbol{C}^{(i)})}{\partial \boldsymbol{C}^{(i)}} \tag{2}$$

Eventually, the balance of linear momentum reads

$$\rho_0^{(i)}\, \ddot{\boldsymbol{\varphi}}^{(i)} = \mathrm{Div}(\boldsymbol{P}^{(i)}) + \boldsymbol{B}^{(i)} \tag{3}$$

where $\boldsymbol{B}^{(i)}$ denotes the body force per reference volume and $\rho_0^{(i)}\, \ddot{\boldsymbol{\varphi}}^{(i)}$ the inertia term using the reference density $\rho_0^{(i)}$. The boundaries are subdivided into the Dirichlet boundary $\Gamma_d^{(i)}$, the Neumann



DOI: 10.1002/nme

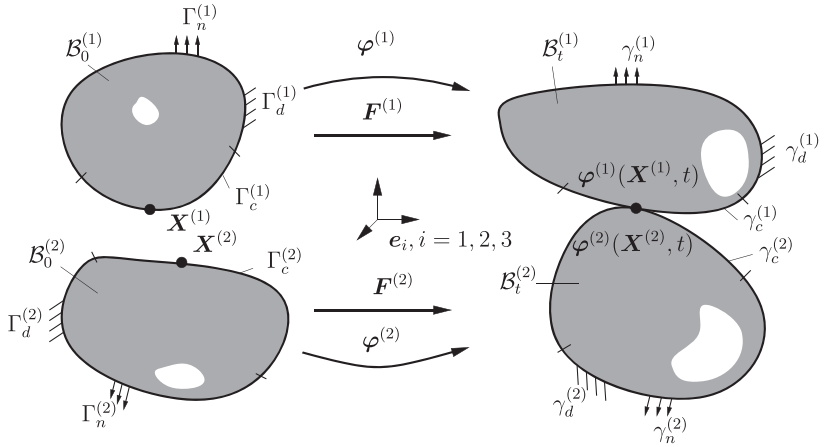


Figure 1. Configurations of the two body contact problem ($\mathcal{B}_0^{(i)}$: bodies in the reference (material) configuration, $\mathcal{B}_t^{(i)}$: bodies in the current (spatial) configuration).

boundary $\Gamma_n^{(i)}$, and the contact boundary $\Gamma_c^{(i)}$ (Figure 1). We require that these boundaries do not overlap; hence, they satisfy

$$\partial\mathcal{B}_0^{(i)} = \Gamma_n^{(i)} \cup \Gamma_c^{(i)} \cup \Gamma_d^{(i)} \quad \text{and} \quad \Gamma_n^{(i)} \cap \Gamma_c^{(i)} = \Gamma_n^{(i)} \cap \Gamma_d^{(i)} = \Gamma_c^{(i)} \cap \Gamma_d^{(i)} = \emptyset \tag{4}$$

Moreover, appropriate boundary conditions are given by

$$\boldsymbol{\varphi}^{(i)} = \bar{\boldsymbol{\varphi}}^{(i)} \quad \text{on } \Gamma_d^{(i)} \; \forall\, t \in \mathcal{I} \tag{5}$$

$$\boldsymbol{P}^{(i)}\, \boldsymbol{N}^{(i)} = \bar{\boldsymbol{T}}^{(i)} \quad \text{on } \Gamma_n^{(i)} \; \forall\, t \in \mathcal{I} \tag{6}$$

where $\boldsymbol{N}^{(i)}$ denotes the unit outward normal. We assume that the bodies are in contact within the considered time interval $t \in \mathcal{I}$ and restrict our consideration on a two body contact problem neglecting self-contact for simplicity of exposition. Additionally, we provide the initial conditions

$$\boldsymbol{\varphi}^{(i)}(0) = \boldsymbol{\varphi}_0^{(i)} \quad \text{in } \mathcal{B}_0^{(i)} \tag{7}$$

$$\dot{\boldsymbol{\varphi}}^{(i)}(0) = \dot{\boldsymbol{\varphi}}_0^{(i)} \quad \text{in } \mathcal{B}_0^{(i)} \tag{8}$$

finalizing the strong form of the problem. Next, we rewrite the system in weak form to obtain the virtual work of the whole system. To this end, we define the solution space

$$\mathcal{V}_s^{(i)} = \left\{ \boldsymbol{\varphi}^{(i)} \in H^1(\mathcal{B}^{(i)}) : \boldsymbol{\varphi}^{(i)} = \bar{\boldsymbol{\varphi}}^{(i)} \text{ on } \Gamma_d^{(i)} \right\} \tag{9}$$

and the space of test functions

$$\mathcal{V}_t^{(i)} = \left\{ \delta\boldsymbol{\varphi}^{(i)} \in H^1(\mathcal{B}^{(i)}) : \delta\boldsymbol{\varphi}^{(i)} = \boldsymbol{0} \text{ on } \Gamma_d^{(i)} \right\} \tag{10}$$

where the Sobolev space $H^1(\mathcal{B}^{(i)})$ consists of square-integrable functions and square-integrable first derivatives thereof. The virtual work contribution of each body reads

$$\begin{aligned} G^{(i)}(\boldsymbol{\varphi}^{(i)}, \delta\boldsymbol{\varphi}^{(i)}) = &\int_{\mathcal{B}_0^{(i)}} \rho_0^{(i)}\, \ddot{\boldsymbol{\varphi}}^{(i)} \cdot \delta\boldsymbol{\varphi}^{(i)}\, \mathrm{d}V + \int_{\mathcal{B}_0^{(i)}} \boldsymbol{F}^{(i)} \boldsymbol{S}^{(i)} : \mathrm{Grad}(\delta\boldsymbol{\varphi}^{(i)})\, \mathrm{d}V - \\ &\int_{\mathcal{B}_0^{(i)}} \bar{\boldsymbol{B}}^{(i)} \cdot \delta\boldsymbol{\varphi}^{(i)}\, \mathrm{d}V - \int_{\Gamma_n^{(i)}} \bar{\boldsymbol{T}}^{(i)} \cdot \delta\boldsymbol{\varphi}^{(i)}\, \mathrm{d}A - \int_{\Gamma_c^{(i)}} \boldsymbol{t}^{(i)} \cdot \delta\boldsymbol{\varphi}^{(i)}\, \mathrm{d}A \end{aligned} \tag{11}$$



DOI: 10.1002/nme

for $\delta\boldsymbol{\varphi}^{(i)} \in \mathcal{V}_t^{(i)}$ and $\boldsymbol{\varphi}^{(i)} \in \mathcal{V}_s^{(i)}$. Here, $\boldsymbol{S}$ denotes the second Piola–Kirchhoff stress tensor. Now, the principle of virtual work for the two-body contact problem under consideration can be written as $G = \sum_{i=1}^{2} G^{(i)} = 0$. Taking into account the balance of linear momentum across the contact interface

$$-\boldsymbol{t}^{(2)}\,\mathrm{d}A = \boldsymbol{t}^{(1)}\,\mathrm{d}A \tag{12}$$

the contact contribution to the virtual work can be summarized in the expression

$$G^c(\boldsymbol{\varphi}, \delta\boldsymbol{\varphi}) = \sum_{i=1}^{2} G^{(i),c}\left(\boldsymbol{\varphi}^{(i)}, \delta\boldsymbol{\varphi}^{(i)}\right) = \int_{\Gamma_c^{(1)}} \boldsymbol{t}^{(1)} \cdot \left[\delta\boldsymbol{\varphi}^{(1)} - \delta\boldsymbol{\varphi}^{(2)}\right] \mathrm{d}A \tag{13}$$

In the last statement, $\boldsymbol{\varphi}$ contains the collection of the mappings $\boldsymbol{\varphi}^{(i)}$, $i = 1, 2$ (similarly for $\delta\boldsymbol{\varphi}$).

### 2.1. Contact formulation

We assume that a point $\boldsymbol{\varphi}^{(1)}(\boldsymbol{X}^{(1)}, t) \in \gamma_c^{(1)}$, $\gamma_c^{(1)} = \boldsymbol{\varphi}\left(\Gamma_c^{(1)}\right)$ on the surface $\gamma_c^{(1)}$ is in contact with the opposing master surface $\gamma_c^{(2)}$ and define the projection

$$\|\boldsymbol{\varphi}^{(1)}(\boldsymbol{X}^{(1)}) - \boldsymbol{\varphi}^{(2)}\left(\bar{\boldsymbol{X}}^{(2)}(\boldsymbol{X}^{(1)})\right)\| \to \min \tag{14}$$

where $\boldsymbol{\varphi}^{(2)}\left(\bar{\boldsymbol{X}}^{(2)}(\boldsymbol{X}^{(1)})\right)$ is the closest point to $\boldsymbol{\varphi}^{(1)}(\boldsymbol{X}^{(1)})$. The master surface $\gamma_c^{(2)}$ itself can be viewed as a 2D manifold parametrized by the convective coordinates $\xi^\alpha$, $\alpha \in \{1, 2\}$. Thus, the projection can be characterized by the relationships

$$\bar{\boldsymbol{X}}^{(2)}(\boldsymbol{X}^{(1)}) := \boldsymbol{X}^{(2)}(\bar{\boldsymbol{\xi}}) \tag{15}$$

and

$$\bar{\boldsymbol{\varphi}}^{(2)} := \boldsymbol{\varphi}^{(2)}(\bar{\boldsymbol{\xi}}), \quad \bar{\boldsymbol{\xi}} = \left[\bar{\xi^1}, \bar{\xi^2}\right] \tag{16}$$

where $\bar{\xi}^\alpha$ are calculated from (14). We further introduce tangent vectors

$$\boldsymbol{a}_\alpha := \boldsymbol{\varphi}^{(2)}_{,\alpha}(\bar{\boldsymbol{\xi}}) \tag{17}$$

where $(\bullet)_{,\alpha}$ denotes the derivative with respect to $\xi^\alpha$. Note that the vectors $\boldsymbol{a}_\alpha$ are directed tangentially along the coordinate curves $\xi^\alpha$ at $\bar{\boldsymbol{\varphi}}^{(2)}$ (Figure 2). Associated dual vectors are defined by

$$\boldsymbol{a}^\alpha = m^{\alpha\beta}\boldsymbol{a}_\beta \tag{18}$$

where $m^{\alpha\beta} = (m_{\alpha\beta})^{-1}$ is the inverse of the metric $m_{\alpha\beta} = \boldsymbol{a}_\alpha \cdot \boldsymbol{a}_\beta$. Next, we introduce the gap function

$$g = \left(\boldsymbol{\varphi}^{(1)} - \bar{\boldsymbol{\varphi}}^{(2)}\right) \cdot \boldsymbol{n} \tag{19}$$

where $\boldsymbol{n}$ denotes the unit outward normal to $\gamma_c^{(2)}$ at $\bar{\boldsymbol{\varphi}}^{(2)}$, defined as

$$\boldsymbol{n} = \frac{\boldsymbol{a}_1 \times \boldsymbol{a}_2}{\|\boldsymbol{a}_1 \times \boldsymbol{a}_2\|} \tag{20}$$

Note that the tangent vectors $\boldsymbol{a}_\alpha$ along with the normal vector $\boldsymbol{n}$ are covariant base vectors. Furthermore, the normal vector $\boldsymbol{n}$ is assumed to be directed tangentially along the coordinate line $\xi^3$ (Figure 2). The variation of the gap function can now be written in the form

$$\delta g = \left(\delta\boldsymbol{\varphi}^{(1)} - \delta\bar{\boldsymbol{\varphi}}^{(2)}\right) \cdot \boldsymbol{n} \tag{21}$$



DOI: 10.1002/nme

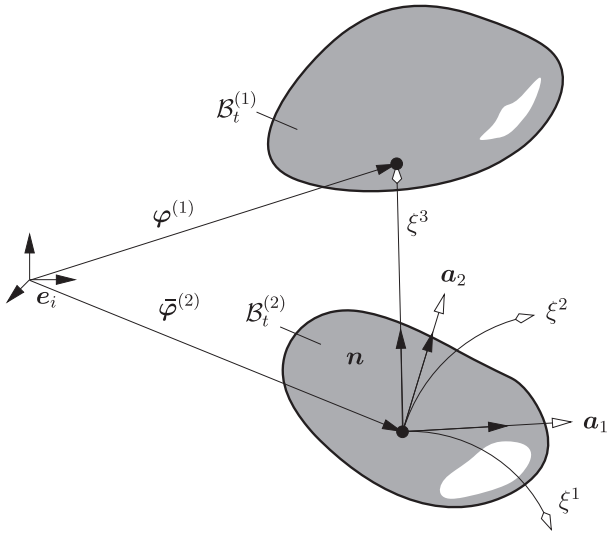


Figure 2. Parametrization of the master surface $\gamma_c^{(2)}$.

As usual, we decompose the contact traction in (13) into the normal and the tangential part

$$\boldsymbol{t}^{(1)} = t_N\,\boldsymbol{n} + \boldsymbol{t}_T \tag{22}$$

and require that $\boldsymbol{t}_T \cdot \boldsymbol{n} = 0$. For the normal component, the Karush–Kuhn–Tucker conditions

$$g \geqslant 0, \quad t_N \leqslant 0, \quad t_N\, g = 0 \tag{23}$$

have to hold, whereas the vector $\boldsymbol{t}_T$ lies in the tangent space of the master surface $\gamma_c^{(2)}$ and can be resolved via

$$\boldsymbol{t}_T = t_{T_\alpha}\boldsymbol{a}^\alpha \tag{24}$$

The corresponding frictional constitutive law to define the tractions $t_{T_\alpha}$ will be dealt with in the appendix.

Summarizing, the contact contribution to the virtual work can now be written in the form

$$G^c(\boldsymbol{\varphi}, \delta\boldsymbol{\varphi}) = \int_{\Gamma_c^{(1)}} \left[\delta\boldsymbol{\varphi}^{(1)} - \delta\bar{\boldsymbol{\varphi}}^{(2)}\right] \cdot \left[t_N\,\boldsymbol{n} + t_{T_\alpha}\boldsymbol{a}^\alpha\right] \mathrm{d}A \tag{25}$$

The last statement depends crucially on the variation of the convective coordinates $\bar{\boldsymbol{\xi}}$ on which we will focus next.

### 2.2. *Frictional kinematics*

Next, we focus on the variation of the convective coordinates to complete the contact formulation given in (25). In particular, we outline the most common approach, referred to as the *direct approach* in the following [23] and present subsequently a new augmentation technique for the description of the frictional kinematics.

**Direct approach** The convective coordinates $\bar{\boldsymbol{\xi}} = \left[\bar{\xi}^1, \bar{\xi}^2\right]$ can be obtained from the solution of the minimum distance problem (14). Correspondingly, the orthogonality condition

$$\left(\boldsymbol{\varphi}^{(1)} - \bar{\boldsymbol{\varphi}}^{(2)}\right) \cdot \boldsymbol{a}_\alpha = 0, \quad \forall\alpha \in \{1, 2\} \tag{26}$$

has to be valid. Computing the time derivative of the last equation yields

$$\left(\dot{\boldsymbol{\varphi}}^{(1)} - \dot{\bar{\boldsymbol{\varphi}}}^{(2)} - \boldsymbol{a}_\beta\dot{\bar{\xi}}^\beta\right) \cdot \boldsymbol{a}_\alpha + \left(\boldsymbol{\varphi}^{(1)} - \bar{\boldsymbol{\varphi}}^{(2)}\right) \cdot \left(\dot{\boldsymbol{a}}_\alpha + \boldsymbol{a}_{\alpha\beta}\dot{\bar{\xi}}^\beta\right) = 0 \tag{27}$$



DOI: 10.1002/nme

Using the unit length of the normal vector, that is, $\boldsymbol{n} \cdot \boldsymbol{n} = 1$ together with $(\boldsymbol{\varphi}^{(1)} - \bar{\boldsymbol{\varphi}}^{(2)}) = g\boldsymbol{n}$, we can rearrange the terms in (27) and obtain the rate of change of the convective coordinates

$$\dot{\bar{\xi}}^{\beta} = A^{\alpha\beta} \left[ \left( \dot{\boldsymbol{\varphi}}^{(1)} - \dot{\bar{\boldsymbol{\varphi}}}^{(2)} \right) \cdot \boldsymbol{a}_{\alpha} + g\, \boldsymbol{n} \cdot \dot{\bar{\boldsymbol{\varphi}}}^{(2)}_{,\alpha} \right] \tag{28}$$

where $A^{\alpha\beta}$ denotes the inverse of $A_{\alpha\beta} := m_{\alpha\beta} - g\, h_{\alpha\beta}$ and $h_{\alpha\beta} = \boldsymbol{a}_{\alpha\beta} \cdot \boldsymbol{n}$ is the curvature of the surface. Replacing the velocity by the variation yields

$$\delta\bar{\xi}^{\beta} = A^{\alpha\beta} \left[ \left( \delta\boldsymbol{\varphi}^{(1)} - \delta\bar{\boldsymbol{\varphi}}^{(2)} \right) \cdot \boldsymbol{a}_{\alpha} + g\, \boldsymbol{n} \cdot \delta\bar{\boldsymbol{\varphi}}^{(2)}_{,\alpha} \right] \tag{29}$$

Assuming that $g = 0$ is valid at the contact interface, the variation of $\bar{\xi}^{\alpha}$ boils down to

$$\delta\bar{\xi}^{\alpha} = \left( \delta\boldsymbol{\varphi}^{(1)} - \delta\bar{\boldsymbol{\varphi}}^{(2)} \right) \cdot \boldsymbol{a}^{\alpha} \tag{30}$$

Accordingly, the virtual work expression (25) can be recast in the form

$$G^{c}(\boldsymbol{\varphi}, \delta\boldsymbol{\varphi}) = \int_{\Gamma_c^{(1)}} \left( t_N \delta g + t_{T_\alpha} \delta\bar{\xi}^{\alpha} \right) \mathrm{d}A \tag{31}$$

where relation (21) has been used. The majority of previous works dealing with large deformation frictional contact problems rely on (31) [2]. Note that statement (31) holds true if (29) is used instead of (30), because the additional terms to be considered only redefine the tractions $t_{T_\alpha}$ in tangential direction.

### *2.3. Coordinate augmentation technique*

Following the arguments in Hesch & Betsch [16], we extend a specific coordinate augmentation technique to frictional contact problems. This technique relies on the introduction of additional coordinates $\mathfrak{f} = [f^1,\ f^2] \in \mathbb{R}^2$ that represent the convective coordinates $[\xi^1,\ \xi^2]$. To link the new coordinates to the original ones, we introduce two constraint functions

$$\boldsymbol{\Phi}^{\mathrm{aug}}(\boldsymbol{\varphi}, \mathfrak{f}) = \begin{bmatrix} \left( \boldsymbol{\varphi}^{(1)} - \boldsymbol{\varphi}^{(2)}(\mathfrak{f}) \right) \cdot \boldsymbol{a}_1(\mathfrak{f}) \\ \left( \boldsymbol{\varphi}^{(1)} - \boldsymbol{\varphi}^{(2)}(\mathfrak{f}) \right) \cdot \boldsymbol{a}_2(\mathfrak{f}) \end{bmatrix} \tag{32}$$

and require that $\boldsymbol{\Phi}^{\mathrm{aug}} = 0$. Similar to definition (17) for the tangent vectors, in (32), $\boldsymbol{a}_{\alpha}(\mathfrak{f}) = \boldsymbol{\varphi}^{(2)}_{,\alpha}(\mathfrak{f})$ for $\alpha = 1, 2$. Analogous to the definition of the gap function (19), we introduce

$$\tilde{g}(\boldsymbol{\varphi}, \mathfrak{f}) = \left( \boldsymbol{\varphi}^{(1)} - \boldsymbol{\varphi}^{(2)}(\mathfrak{f}) \right) \cdot \tilde{\boldsymbol{n}}(\mathfrak{f}) \tag{33}$$

where $\tilde{\boldsymbol{n}}(\mathfrak{f})$ again follows from (20) by replacing $\boldsymbol{a}_{\alpha}$ with $\boldsymbol{\varphi}^{(2)}_{,\alpha}(\mathfrak{f})$. The contact contribution to the virtual work can now be determined along the lines of the direct approach. Accordingly, similar to (31), we obtain

$$G^{c}(\boldsymbol{\varphi}, \mathfrak{f}, \delta\boldsymbol{\varphi}, \delta\mathfrak{f}) = \int_{\Gamma_c^{(1)}} \left( t_N \delta\tilde{g} + t_{T_\alpha} \delta f^{\alpha} \right) \mathrm{d}A \tag{34}$$

where $\delta\tilde{g} = \left( \delta\boldsymbol{\varphi}^{(1)} - \delta\boldsymbol{\varphi}^{(2)}(\mathfrak{f}) \right) \cdot \tilde{\boldsymbol{n}}(\mathfrak{f})$. It is important to realize that the augmented coordinates $\mathfrak{f}$ are to be viewed as primary variables on an equal footing with the original variables $\boldsymbol{\varphi}$. Consequently, the newly proposed augmentation technique strongly affects the discretization in space and time. Indeed, it will be shown in the sequel that the newly proposed augmentation technique simplifies the implementation significantly when compared with the direct approach.



DOI: 10.1002/nme

## 3. SPATIAL DISCRETIZATION

We apply a suitable spatial discretization process to the bodies under consideration and to the contact constraints. More precisely, displacement-based finite elements are used for the bodies in contact, subdividing each body $\mathcal{B}^{(i)}$ into a finite number of elements $n_{el}^{(i)}$ via

$$\mathcal{B}^{(i)} \approx \mathcal{B}^{(i),h} = \bigcup_{e}^{n_{el}^{(i)}} \mathcal{B}_e^{(i),h} \tag{35}$$

The polynomial approximations of the solution and the test space are written as

$$\boldsymbol{\varphi}^{(i),h} = \sum_{I \in \omega} N_I \, \boldsymbol{q}_I^{(i)}, \quad \delta\boldsymbol{\varphi}^{(i),h} = \sum_{J \in \omega} N_J \, \delta\boldsymbol{q}_J^{(i)} \tag{36}$$

where $\boldsymbol{q}_I^{(i)}$ represents the nodal position at point $I \in \omega = \{1, \ldots, n_{\text{node}}\}$ and $\delta\boldsymbol{q}_J^{(i)}$ the corresponding variation at point $J$. Furthermore, $N_I : \mathcal{B}^{(i)} \to \mathbb{R}$ are global trilinear Lagrangian shape functions. The semi-discrete version of the principle of virtual work can now be written in the form

$$\begin{aligned} G^h(\boldsymbol{q}, \delta\boldsymbol{q}) = \sum_i \delta\boldsymbol{q}_I^{(i)} \cdot \Bigg( & \int_{\mathcal{B}^{(i),h}} \rho_0^{(i)} \, N_I \, N_J \, \mathrm{d}V \ddot{\boldsymbol{q}}_J^{(i)} + \int_{\mathcal{B}^{(i),h}} \nabla_{\boldsymbol{X}} \, N_I \cdot \boldsymbol{S}^{(i),h} \nabla_{\boldsymbol{X}} \, N_J \, \mathrm{d}V \boldsymbol{q}_J^{(i)} \\ & - \int_{\mathcal{B}^{(i),h}} N_I \bar{\boldsymbol{B}}^{(i),h} \, \mathrm{d}V - \int_{\Gamma_n^{(i),h}} N_I \bar{\boldsymbol{T}}^{(i),h} \, \mathrm{d}A \Bigg) - G^{c,h} \end{aligned} \tag{37}$$

Note that the nodal position vectors $\boldsymbol{q}_I^{(1)}$ and $\boldsymbol{q}_I^{(2)}$ have been collected in the vector $\boldsymbol{q}$ (similarly for $\delta\boldsymbol{q}$). The last term in (37) denotes the discrete version of the contact virtual work, which will be dealt with in the following section. We can rewrite (37) as follows

$$G^h(\boldsymbol{q}, \delta\boldsymbol{q}) = \sum_i \delta\boldsymbol{q}_I^{(i)} \cdot \left( M^{IJ} \ddot{\boldsymbol{q}}_J^{(i)} + \boldsymbol{f}^{(i),\text{int},I} - \boldsymbol{f}^{(i),\text{ext},I} + \boldsymbol{f}^{(i),\text{c},I} + \boldsymbol{f}^{(i),\text{fric},I} \right) \tag{38}$$

where $M^{IJ}$ represents the nodal mass contributions, $\boldsymbol{f}^{(i),\text{int},I}$ the internal nodal forces, and $\boldsymbol{f}^{(i),\text{ext},I}$ the external forces. Throughout the paper, we assume that the internal and external forces are associated with a potential energy function

$$V(\boldsymbol{q}) = \int_{\mathcal{B}^{(i),h}} W(\boldsymbol{C}^h) \, \mathrm{d}V - \boldsymbol{q}_I \cdot \boldsymbol{f}^{(i),\text{ext},I} \tag{39}$$

The last two terms in (38) represent the normal contact and frictional forces, which will be derived in the next section.

### 3.1. Node-to-surface element

Similar to the approximations of the solution and the test space, we define the following approximations at the contact boundaries

$$\boldsymbol{\varphi}_c^{(i),h} = \sum_{I \in \bar{\omega}} \hat{N}^I \boldsymbol{q}_I^{(i)}, \quad \delta\boldsymbol{\varphi}_c^{(i),h} = \sum_{J \in \bar{\omega}} \hat{N}^J \, \delta\boldsymbol{q}_J^{(i)} \tag{40}$$

where $\hat{N}_I$ denote bilinear shape functions at the corresponding node $I \in \bar{\omega}$, representing the set of all nodes on the contact interface. Using the direct approach, we have to compute the convected coordinates $\bar{\xi}^1$ and $\bar{\xi}^2$ internally within each NTS element $A$ (Figure 3) by solving

$$\begin{bmatrix} \left( \boldsymbol{q}_s^{(1)} - \boldsymbol{q}_s^{(2)} \left( \bar{\xi}^1, \bar{\xi}^2 \right) \right) \cdot \boldsymbol{a}_1 \left( \bar{\xi}^1, \bar{\xi}^2 \right) \\ \left( \boldsymbol{q}_s^{(1)} - \boldsymbol{q}_s^{(2)} \left( \bar{\xi}^1, \bar{\xi}^2 \right) \right) \cdot \boldsymbol{a}_2 \left( \bar{\xi}^1, \bar{\xi}^2 \right) \end{bmatrix} = \boldsymbol{0} \tag{41}$$



DOI: 10.1002/nme

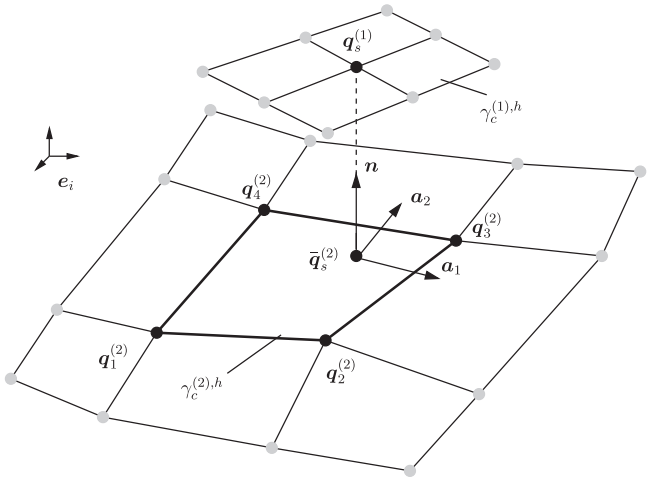


Figure 3. Three-dimensional five node node-to-surface element.

for the convective coordinates using a Newton–Raphson iteration. The discrete nodal gap function $g_s^h$ (Figure 3) reads

$$g_s^h(\boldsymbol{q}_A) = \left(\boldsymbol{q}_s^{(1)} - \boldsymbol{q}_s^{(2)}(\bar{\xi}^1, \bar{\xi}^2)\right) \cdot \boldsymbol{n}\left(\bar{\xi}^1, \bar{\xi}^2\right) \tag{42}$$

using the set of nodes $\eta_{NTS} := \{\boldsymbol{q}_A\} = \left\{\boldsymbol{q}_s^{(1)}, \boldsymbol{q}_1^{(2)}, \boldsymbol{q}_2^{(2)}, \boldsymbol{q}_3^{(2)}, \boldsymbol{q}_4^{(2)}\right\}$. Employing the discrete nodal gap function, we can define the constraint function in normal direction

$$\bar{\Phi}^{\mathrm{n}}(\boldsymbol{q}_A) = \int_{\Gamma_c^{(1)}} g_s^h \, \mathrm{d}A \tag{43}$$

along with the Lagrange multipliers $\bar{\lambda}^n$ that can be viewed as discrete counterpart of the normal traction $t_N$.

The corresponding tangential tractions are dealt with in Appendix A for the case of Coulomb's law. Note that we incorporate the frictional response using a widely used regularization method based on a penalty parameter. Other types of enforcement of the frictional response are possible [24–26], because the proposed augmentation technique remains unaffected by, for example, the existence of additional Lagrange multipliers. The chosen approach is used for the sake of clarity in the presentation.

Similar to the kinematic relationship (29), the variation of the convective coordinates in the discrete setting reads

$$\delta\bar{\xi}_s^{\alpha,h} = A^{\alpha\beta}\left[\left(\delta\boldsymbol{q}_s^{(1)} - \delta\bar{\boldsymbol{q}}_s^{(2)}\right) \cdot \boldsymbol{a}_\beta + g^h \boldsymbol{n} \cdot \delta\boldsymbol{a}_\beta\right] \tag{44}$$

If we assume that the gap is zero, we obtain

$$\delta\bar{\xi}_s^{\alpha,h} = A^{\alpha\beta}\left(\delta\boldsymbol{q}_s^{(1)} - \delta\bar{\boldsymbol{q}}_s^{(2)}\right) \cdot \boldsymbol{a}_\beta \tag{45}$$

and the corresponding discrete virtual contact work for a single NTS element reads

$$G_s^{c,h} = \int_{\Gamma_c^{(1)}} \left(t_N \delta g_s^h + t_{T_\alpha} \delta\bar{\xi}_s^{\alpha,h}\right) \mathrm{d}A \tag{46}$$



DOI: 10.1002/nme

With regard to (38), we rearrange the frictional contributions using a single vector $\delta \boldsymbol{q} \cdot \boldsymbol{f}^{\text{fric}}$. Furthermore, we collect all normal constraints in a single vector $\boldsymbol{\Phi}^n(\boldsymbol{q})$ and assemble the associated Lagrange multipliers in the vector $\boldsymbol{\lambda}^{\text{n}}$. Then, the semi-discrete equations of motion read

$$\begin{aligned} \mathbf{0} &= \boldsymbol{M}\ddot{\boldsymbol{q}} + \nabla_{\boldsymbol{q}}\, V(\boldsymbol{q}) + \nabla_{\boldsymbol{q}}\, (\boldsymbol{\Phi}^{\text{n}}(\boldsymbol{q}) \cdot \boldsymbol{\lambda}^{\text{n}}) + \boldsymbol{f}^{\text{fric}}(\boldsymbol{q}) \\ \mathbf{0} &= \boldsymbol{\Phi}^{\text{n}}(\boldsymbol{q}) \end{aligned} \tag{47}$$

where $\boldsymbol{M}$ denotes the consistent mass matrix.

### *3.2. Coordinate augmentation technique*

Next, we apply the coordinate augmentation technique described in Section 2.3 to the NTS element. In contrast to the direct approach, we calculate the convective coordinates on a global level, that is, we do not solve the algebraic system of equations in (41) internally but enforce them as additional constraints

$$\bar{\boldsymbol{\Phi}}^{\text{aug}}(\boldsymbol{q}_A, \mathfrak{f}_A) = \begin{bmatrix} \left(\boldsymbol{q}^{(1)} - \boldsymbol{q}^{(2)}(\mathfrak{f}_A)\right) \cdot \boldsymbol{a}_1(\mathfrak{f}_A) \\ \left(\boldsymbol{q}^{(1)} - \boldsymbol{q}^{(2)}(\mathfrak{f}_A)\right) \cdot \boldsymbol{a}_2(\mathfrak{f}_A) \end{bmatrix} \tag{48}$$

Here, we make use of a vector $\mathfrak{f}_A \in \mathbb{R}^2$ for each NTS element, representing the convective coordinates $\left[\bar{\xi}^1, \bar{\xi}^2\right]$. The associated Lagrange multipliers are given by $\bar{\boldsymbol{\lambda}}^{\text{aug}}$. In addition to that, the constraints in normal direction are given by

$$\bar{\Phi}^{\text{n}}(\boldsymbol{q}_A, \mathfrak{f}_A) = \left(\boldsymbol{q}_s^{(1)} - \boldsymbol{q}_s^{(2)}(\mathfrak{f}_A)\right) \cdot \boldsymbol{n}(\mathfrak{f}_A) \tag{49}$$

As before, we collect all data in global vectors, that is, we collect all augmented coordinates in a single vector $\mathfrak{f} \in \mathbb{R}^l$, where $l$ denotes the number of all convective coordinates. Furthermore, the augmented constraints (48) are arranged in a single vector $\boldsymbol{\Phi}^{\text{aug}}(\boldsymbol{q}, \mathfrak{f}) \in \mathbb{R}^l$ and the associated Lagrange multipliers in a single vector $\boldsymbol{\lambda}^{\text{aug}} \in \mathbb{R}^l$. The semi-discrete equations of motion can now be written as follows

$$\begin{aligned} \mathbf{0} &= \boldsymbol{M}\ddot{\boldsymbol{q}} + \nabla_{\boldsymbol{q}} V(\boldsymbol{q}) + \nabla_{\boldsymbol{q}}(\boldsymbol{\Phi}(\boldsymbol{q}, \mathfrak{f}) \cdot \boldsymbol{\lambda}) \\ \mathbf{0} &= \nabla_{\mathfrak{f}}(\boldsymbol{\Phi}(\boldsymbol{q}, \mathfrak{f}) \cdot \boldsymbol{\lambda}) + \boldsymbol{f}^{\text{aug}}(\boldsymbol{q}, \mathfrak{f}) \\ \mathbf{0} &= \boldsymbol{\Phi}(\boldsymbol{q}, \mathfrak{f}) \end{aligned} \tag{50}$$

where $\boldsymbol{\Phi}(\boldsymbol{q}, \mathfrak{f}) = [\boldsymbol{\Phi}^{\text{aug}}, \boldsymbol{\Phi}^{\text{n}}]^T \in \mathbb{R}^m$ and $\boldsymbol{\lambda} = [\boldsymbol{\lambda}^{\text{aug}}, \boldsymbol{\lambda}^{\text{n}}]^T \in \mathbb{R}^m$. Furthermore, $\boldsymbol{f}^{\text{aug}}(\boldsymbol{q}, \mathfrak{f}) = [t_{T_1}, \ldots, t_{T_n}]^T \in \mathbb{R}^l$ combines the frictional tractions in a single vector.

**Implementation** To implement the newly proposed method in an efficient way, we eliminate the additional Lagrange multipliers $\boldsymbol{\lambda}^{\text{aug}}$ using the algebraic condition $(50)_2$. For a single NTS element, this condition reads

$$\nabla_{\mathfrak{f}_{\text{A}}} \left(\bar{\boldsymbol{\Phi}}^{\text{aug}} \cdot \bar{\boldsymbol{\lambda}}^{\text{aug}}\right) + \nabla_{\mathfrak{f}_{\text{A}}}\, \bar{\Phi}^n \bar{\lambda}^n + \bar{\boldsymbol{f}}^{\text{aug}} = \mathbf{0} \tag{51}$$

where $\bar{\boldsymbol{f}}^{\text{aug}} = [t_{T_1}, t_{T_2}]^T \in \mathbb{R}^2$ represents the tangential tractions of the corresponding NTS element. The Lagrange multipliers can now be calculated analytically as follows

$$\bar{\boldsymbol{\lambda}}^{\text{aug}} = -\left(\nabla_{\mathfrak{f}_{\text{A}}} \bar{\boldsymbol{\Phi}}^{\text{aug}}\right)^{-1} \cdot \left(\nabla_{\mathfrak{f}_{\text{A}}} \bar{\Phi}^n \bar{\lambda}^n + \bar{\boldsymbol{f}}^{\text{aug}}\right) \tag{52}$$

Accordingly, on the level of each NTS element, the Lagrange multipliers associated with the augmented coordinates can be expressed in terms of the extended set of coordinates $\boldsymbol{q}_A$, $\mathfrak{f}_A$ and the contact traction $\bar{\lambda}^n$ in normal direction. Using (52) for each NTS element, the vector $\bar{\boldsymbol{\lambda}}^{\text{aug}}$ of Lagrange multipliers can be eliminated from the semi-discrete equations of motion (50). Accordingly, we arrive at

$$\begin{aligned} \mathbf{0} &= \boldsymbol{M}\ddot{\boldsymbol{q}} + \nabla_{\boldsymbol{q}} V(\boldsymbol{q}) + (\mathfrak{B}\nabla_{\mathfrak{f}} \boldsymbol{\Phi}^n(\boldsymbol{q}, \mathfrak{f}) + \nabla_{\boldsymbol{q}} \boldsymbol{\Phi}^n(\boldsymbol{q}, \mathfrak{f})) \cdot \boldsymbol{\lambda}^n + \mathfrak{B}\boldsymbol{f}^{\text{aug}}(\boldsymbol{q}, \mathfrak{f}) \\ \mathbf{0} &= \boldsymbol{\Phi}(\boldsymbol{q}, \mathfrak{f}) \end{aligned} \tag{53}$$



DOI: 10.1002/nme

where the block diagonal matrix $\mathfrak{P} = \mathrm{diag}(\bar{\mathfrak{P}}_1, \ldots, \bar{\mathfrak{P}}_n)$ consists of the local projection matrix

$$\bar{\mathfrak{P}} = -\nabla_{\boldsymbol{q}_A} \bar{\boldsymbol{\Phi}}^{\mathrm{aug}} \left( \nabla_{\mathfrak{f}_A} \bar{\boldsymbol{\Phi}}^{\mathrm{aug}} \right)^{-1} \tag{54}$$

for each NTS element. Note that $\nabla_{\mathfrak{f}} \boldsymbol{\Phi}^n = \boldsymbol{0}$ is valid at the solution point, and we obtain the simplified system

$$\begin{aligned} \boldsymbol{0} &= \boldsymbol{M}\ddot{\boldsymbol{q}} + \nabla_{\boldsymbol{q}} V(\boldsymbol{q}) + \nabla_{\boldsymbol{q}} (\boldsymbol{\Phi}^n(\boldsymbol{q}, \mathfrak{f}) \cdot \boldsymbol{\lambda}^n) + \mathfrak{P} \boldsymbol{f}^{\mathrm{aug}}(\boldsymbol{q}, \mathfrak{f}) \\ \boldsymbol{0} &= \boldsymbol{\Phi}(\boldsymbol{q}, \mathfrak{f}) \end{aligned} \tag{55}$$

The last set of equations defines the residual $[\boldsymbol{R}_q, \boldsymbol{\Phi}]^{\mathrm{T}}$, which we have to solve with respect to $\boldsymbol{q} \in \mathbb{R}^n$, $\mathfrak{f} \in \mathbb{R}^l$, and $\boldsymbol{\lambda}^n \in \mathbb{R}^{m-l}$. This first reduction step can be written in matrix notation using the modified projection matrix

$$\widetilde{\mathcal{P}} = \begin{bmatrix} \boldsymbol{I}^{n\times n} & \mathfrak{P} & \boldsymbol{0}^{n\times m} \\ \boldsymbol{0}^{m\times n} & \boldsymbol{0}^{m\times l} & \boldsymbol{I}^{m\times m} \end{bmatrix} \in \mathbb{R}^{(n+m)\times(n+l+m)} \tag{56}$$

where $n$ denotes the number of degrees of freedom of the configuration $\boldsymbol{q}$, $m$ the number of constraints $\boldsymbol{\Phi} = [\boldsymbol{\Phi}^{\mathrm{aug}}, \boldsymbol{\Phi}^{\mathrm{n}}]$, and $l$ the number of augmented coordinates $\mathfrak{f}$. Premultiplication of (50) by the projection matrix in (56) yields (55).

In a second step, we eliminate the augmented coordinates within the Newton–Raphson iteration

$$\begin{bmatrix} \boldsymbol{K}_{qq} & \boldsymbol{K}_{q\mathfrak{f}} & \nabla_{\boldsymbol{q}} \boldsymbol{\Phi}^n \\ \nabla_{\boldsymbol{q}}{}^T \boldsymbol{\Phi} & \nabla_{\mathfrak{f}}{}^T \boldsymbol{\Phi} & \boldsymbol{0} \end{bmatrix} \cdot \begin{bmatrix} \Delta \boldsymbol{q} \\ \Delta \mathfrak{f} \\ \Delta \boldsymbol{\lambda}^n \end{bmatrix} = \begin{bmatrix} \boldsymbol{R}_q \\ \boldsymbol{\Phi} \end{bmatrix} \tag{57}$$

that is used to solve (55). Here, $\boldsymbol{K}_{qq}$ and $\boldsymbol{K}_{q\mathfrak{f}}$ denotes the derivative of $\boldsymbol{R}_{\boldsymbol{q}}$ with respect to $\boldsymbol{q}$ and $\mathfrak{f}$, respectively. Next, we extract the equations for the augmented constraints of a single NTS element from (57)

$$\nabla_{\boldsymbol{q}_A}{}^T \bar{\boldsymbol{\Phi}}^{\mathrm{aug}} \Delta \boldsymbol{q}_A + \nabla_{\mathfrak{f}_A}{}^T \bar{\boldsymbol{\Phi}}^{\mathrm{aug}} \Delta \mathfrak{f}_A = \bar{\boldsymbol{\Phi}}^{\mathrm{aug}} \tag{58}$$

and solve this last equation with respect to $\Delta \mathfrak{f}_A$, such that we obtain

$$\begin{aligned} \Delta \mathfrak{f}_A &= \left( \nabla_{\mathfrak{f}_A}{}^T \bar{\boldsymbol{\Phi}}^{\mathrm{aug}} \right)^{-1} \bar{\boldsymbol{\Phi}}^{\mathrm{aug}} - \left( \nabla_{\mathfrak{f}_A}{}^T \bar{\boldsymbol{\Phi}}^{\mathrm{aug}} \right)^{-1} \nabla_{\boldsymbol{q}_A}{}^T \bar{\boldsymbol{\Phi}}^{\mathrm{aug}} \Delta \boldsymbol{q}_A \\ &= \left( \nabla_{\mathfrak{f}_A}{}^T \bar{\boldsymbol{\Phi}}^{\mathrm{aug}} \right)^{-1} \bar{\boldsymbol{\Phi}}^{\mathrm{aug}} + \bar{\mathfrak{P}}^T \Delta \boldsymbol{q}_A \end{aligned} \tag{59}$$

Insertion in (57) yields the reduced system

$$\begin{bmatrix} \boldsymbol{K}_{qq} + \boldsymbol{K}_{q\mathfrak{f}} \mathfrak{P}^T & \nabla_{\boldsymbol{q}} \boldsymbol{\Phi}^n \\ \nabla_{\boldsymbol{q}}{}^T \boldsymbol{\Phi}^n & \boldsymbol{0} \end{bmatrix} \cdot \begin{bmatrix} \Delta \boldsymbol{q} \\ \Delta \boldsymbol{\lambda}^n \end{bmatrix} = \begin{bmatrix} \boldsymbol{R}_q - \boldsymbol{K}_{q\mathfrak{f}} \left( \nabla_{\mathfrak{f}}{}^T \bar{\boldsymbol{\Phi}}^{\mathrm{aug}} \right)^{-1} \boldsymbol{\Phi}^{\mathrm{aug}} \\ \boldsymbol{\Phi}^n \end{bmatrix} \tag{60}$$

The last reduction step can also be written in matrix notation using

$$\bar{\mathcal{P}} = \begin{bmatrix} \boldsymbol{I}^{n\times n} & \mathfrak{P} & \boldsymbol{0}^{n\times(m-l)} \\ \boldsymbol{0}^{(m-l)\times n} & \boldsymbol{0}^{(m-l)\times l} & \boldsymbol{I}^{(m-l)\times(m-l)} \end{bmatrix} \in \mathbb{R}^{(n+m-l)\times(n+m)} \tag{61}$$

It is important to remark that the whole reduction procedure can be carried out on element level for each single NTS-element, because $\mathfrak{P}$ is block diagonal. The convective coordinates can be recovered using (59). The consistent linearization can now be carried out in two different ways:

1. As shown in (57), we have to linearize $(55)_1$ with respect to the configuration $\boldsymbol{q}$ and the augmented coordinates $\mathfrak{f}$. The involved constraints (48) and (49) are at most quadratic in the configuration and in the augmented coordinates, thus the only terms of higher order to be derived depending on the used constitutive law $\boldsymbol{f}^{\mathrm{aug}}$ (this derivative is always necessary) and the $2 \times 2$ inverse matrix $\left( \nabla_{\mathfrak{f}_A}{}^T \bar{\boldsymbol{\Phi}}^{\mathrm{aug}} \right)^{-1}$, that is, we have to linearize $\mathfrak{P}$.



DOI: 10.1002/nme

2. In (55), we have used the projection matrix $\widetilde{\mathcal{P}}$ to obtain a new residual, which we have to linearize to obtain the $(n+m)\times(n+m)$ matrix in (57). Alternatively, we can premultiply the full linearized original system (50) by $\widetilde{\mathcal{P}}$ and obtain

$$\begin{bmatrix} \boldsymbol{K}^o_{qq} + \mathfrak{B}\boldsymbol{K}^o_{\mathfrak{f}q} & \boldsymbol{K}^o_{q\mathfrak{f}} + \mathfrak{B}\boldsymbol{K}^o_{\mathfrak{f}\mathfrak{f}} & \nabla_{\boldsymbol{q}}\boldsymbol{\Phi} + \mathfrak{B}\nabla_{\mathfrak{f}}\boldsymbol{\Phi} \\ \nabla_{\boldsymbol{q}}{}^T\boldsymbol{\Phi} & \nabla_{\mathfrak{f}}{}^T\boldsymbol{\Phi} & \boldsymbol{0} \end{bmatrix} \cdot \begin{bmatrix} \Delta\boldsymbol{q} \\ \Delta\mathfrak{f} \\ \Delta\boldsymbol{\lambda} \end{bmatrix} = \widetilde{\mathcal{P}} \begin{bmatrix} \boldsymbol{R}^o_q \\ \boldsymbol{R}^o_{\mathfrak{f}} \\ \boldsymbol{\Phi} \end{bmatrix} \tag{62}$$

where terms labeled by the upper index $(\bullet)^o$ represent the contributions arising from $(50)_1$ and $(50)_2$. Next, we remove $\Delta\boldsymbol{\lambda}^{\text{aug}}$ and the corresponding columns from the system, because we solve directly for $\boldsymbol{\lambda}^{\text{aug}}$ using (52). The second reduction step follows as before, now avoiding the linearization of $\mathfrak{B}$. Note that we take again advantage of its block diagonal structure, such that all steps can be carried for each contact element.

The linearization is extremely simplified, compared with traditional methods, where we need to calculate the linearization of the variation of the convective coordinates (cf. Laursen [1])

$$\begin{aligned} \Delta\,\delta\bar{\xi}^{\alpha} = & A^{\alpha\beta}\Big[-\boldsymbol{a}_{\beta}\left(\delta\bar{\xi}^{\gamma}\,\Delta\bar{\boldsymbol{\varphi}}^{(2)}_{,\gamma} + \delta\bar{\boldsymbol{\varphi}}^{(2)}_{,\gamma}\,\Delta\bar{\xi}^{\gamma}\right) - \left(\boldsymbol{a}_{\beta}\cdot\boldsymbol{a}_{\gamma\delta} - g\,\boldsymbol{n}\cdot\boldsymbol{a}_{\beta\gamma\delta}\right)\delta\bar{\xi}^{\gamma}\,\Delta\bar{\xi}^{\delta} + \\ & g\left(\delta\bar{\boldsymbol{\varphi}}_{,\beta\gamma}\,\Delta\bar{\xi}^{\gamma} + \Delta\bar{\boldsymbol{\varphi}}_{,\beta\gamma}\,\delta\bar{\xi}^{\gamma}\right)\boldsymbol{n} - \left(\delta\bar{\boldsymbol{\varphi}}^{(2)}_{,\beta} + \boldsymbol{a}_{\beta\gamma}\,\delta\bar{\xi}^{\gamma}\right)\cdot\boldsymbol{a}_{\delta}\,\Delta\bar{\xi}^{\delta} - \\ & \left(\Delta\bar{\boldsymbol{\varphi}}^{(2)}_{,\beta} + \boldsymbol{a}_{\beta\gamma}\,\Delta\bar{\xi}^{\gamma}\right)\cdot\boldsymbol{a}_{\delta}\,\delta\bar{\xi}^{\delta} + \left(\delta\boldsymbol{\varphi}^{(1)} - \delta\bar{\boldsymbol{\varphi}}^{(2)}\right)\left(\Delta\bar{\boldsymbol{\varphi}}^{(2)}_{,\beta} + \boldsymbol{a}_{\beta\gamma}\,\Delta\bar{\xi}^{\gamma}\right) + \\ & \left(\Delta\boldsymbol{\varphi}^{(1)} - \Delta\bar{\boldsymbol{\varphi}}^{(2)}\right)\left(\delta\bar{\boldsymbol{\varphi}}^{(2)}_{,\beta} + \boldsymbol{a}_{\beta\gamma}\,\delta\bar{\xi}^{\gamma}\right)\Big] \end{aligned} \tag{63}$$

where $\Delta\bar{\xi}$ has the same structure as $\delta\bar{\xi}$, given in (29).

**Remark:** Although we use Lagrange multipliers to enforce the normal constraints, we can also apply an augmented Lagrangian method to calculate the exact values of $\boldsymbol{\lambda}^n$.

### *3.3. Conservation properties*

The conservation properties of the underlying mechanical system are well known, so we concentrate on the contact contributions. Reconsider the virtual work contributions of a single contact element

$$\begin{aligned} G^{c,h}(\boldsymbol{q},\delta\boldsymbol{q}) = & \int_{\Gamma_c^{(1)}} t_N\boldsymbol{n}\cdot\left(\delta\boldsymbol{q}^{(1)}_s - \delta\boldsymbol{q}^{(2)}_s\right) + \\ & t_{T_\alpha}A^{\alpha\beta}\left[\left(\delta\boldsymbol{q}^{(1)}_s - \delta\boldsymbol{q}\right)^{(1)}_s\cdot\boldsymbol{a}_{\beta} + g^h\boldsymbol{n}\cdot\delta\boldsymbol{a}_{\beta}\right]\mathrm{d}A = 0 \end{aligned} \tag{64}$$

where we make use of (46) along with (42) and (44). The conservation of linear momentum may be verified by substituting $\delta\boldsymbol{q}_I = \boldsymbol{\eta}$, where $\boldsymbol{\eta}\in\mathbb{R}^3$ is arbitrary and constant into the global virtual work of the constraint forces

$$\begin{aligned} G^{c,h}(\boldsymbol{q},[\boldsymbol{\eta}]) = & \int_{\Gamma_c^{(1)}} t_N\boldsymbol{n}\cdot(\boldsymbol{\eta}-\boldsymbol{\eta}) + \\ & t_{T_\alpha}A^{\alpha\beta}\left[(\boldsymbol{\eta}-\boldsymbol{\eta})\cdot\boldsymbol{a}_{\beta} + g^h\boldsymbol{n}\cdot\sum_I\hat{N}^I_{,\beta}\boldsymbol{\eta}\right]\mathrm{d}A = 0 \end{aligned} \tag{65}$$



DOI: 10.1002/nme

using the direct approach in (44). To verify conservation of angular momentum, we substitute $\delta \boldsymbol{q}_I = \boldsymbol{\eta} \times \boldsymbol{q}_I$ and obtain

$$\begin{aligned} G^{c,h}(\boldsymbol{q}, [\boldsymbol{\eta} \times \boldsymbol{q}_I]) &= -\boldsymbol{\eta} \cdot \int\limits_{\Gamma_c^{(1)}} t_N \boldsymbol{n} \times \left( \boldsymbol{q}_s^{(1)} - \bar{\boldsymbol{q}}_s^{(2)} \right) + \\ &\qquad t_{T_\alpha} A^{\alpha\beta} \left[ \boldsymbol{a}_\beta \times \left( \boldsymbol{q}_s^{(1)} - \bar{\boldsymbol{q}}_s^{(2)} \right) + g^h \boldsymbol{n} \times \boldsymbol{a}_\beta \right] \mathrm{d}A \\ &= -\boldsymbol{\eta} \cdot \int\limits_{\Gamma_c^{(1)}} t_N \boldsymbol{n} \times g^h \boldsymbol{n} + \\ &\qquad t_{T_\alpha} A^{\alpha\beta} \left[ g^h \boldsymbol{a}_\beta \times \boldsymbol{n} + g^h \boldsymbol{n} \times \boldsymbol{a}_\beta \right] \mathrm{d}A = 0 \end{aligned} \tag{66}$$

Note that the simplified variation (45) conserves angular momentum only if the normal gap is equal zero.

Finally, we verify the conservation properties of the augmented system in (50). The corresponding contact virtual work reads

$$G^{c,h}(\boldsymbol{q}, \delta\boldsymbol{q}, \bar{\mathbf{f}}) = \delta\boldsymbol{q} \cdot \nabla_{\boldsymbol{q}} \left( \boldsymbol{\Phi}(\boldsymbol{q}, \bar{\mathbf{f}}) \cdot \boldsymbol{\lambda} \right) \tag{67}$$

where we have taken $(50)_1$ into account. Insertion of $\delta \boldsymbol{q}_I = \boldsymbol{\eta}$ into the augmented system yields

$$G^{c,h}(\boldsymbol{q}, [\eta], \bar{\mathbf{f}}) = \eta \cdot \sum_I \nabla_{\boldsymbol{q}_I} \left( \boldsymbol{\Phi}(\boldsymbol{q}, \bar{\mathbf{f}}) \cdot \boldsymbol{\lambda} \right) \tag{68}$$

whereas insertion of $\delta \boldsymbol{q}_I = \boldsymbol{\eta} \times \boldsymbol{q}_I$ yields

$$G^{c,h}(\boldsymbol{q}, [\boldsymbol{\eta} \times \boldsymbol{q}_I], \bar{\mathbf{f}}) = \eta \cdot \sum_I \boldsymbol{q}_I \times \nabla_{\boldsymbol{q}_I} \left( \boldsymbol{\Phi}(\boldsymbol{q}, \bar{\mathbf{f}}) \cdot \boldsymbol{\lambda} \right) \tag{69}$$

Because the constraints are frame indifferent with respect to rigid body motions of the form

$$\bar{\boldsymbol{q}}_I^\sharp = \boldsymbol{c} + \boldsymbol{Q} \bar{\boldsymbol{q}}_I \tag{70}$$

where $\boldsymbol{c} \in \mathbb{R}^3$ is a constant vector $\boldsymbol{Q} \in SO(3)$, we can show that for each NTS element, the relation

$$\bar{\boldsymbol{\Phi}} \left( \bar{\boldsymbol{q}}^\sharp, \bar{\mathbf{f}} \right) = \bar{\boldsymbol{\Phi}} \left( \bar{\boldsymbol{q}}, \bar{\mathbf{f}} \right) \tag{71}$$

is valid. Substituting $\boldsymbol{c} = \epsilon \boldsymbol{\eta}$, $\boldsymbol{\eta} \in \mathbb{R}^3$, $\boldsymbol{Q} = \boldsymbol{I}$ and subsequent derivation with respect to $\epsilon$ yields

$$\mathbf{0} = \left. \frac{\mathrm{d}}{\mathrm{d}\epsilon} \right|_{\epsilon=0} \bar{\boldsymbol{\Phi}} \left( \bar{\boldsymbol{q}}^\sharp, \bar{\mathbf{f}} \right) = \eta \cdot \sum_I \nabla_{\boldsymbol{q}_I} \bar{\boldsymbol{\Phi}} \left( \bar{\boldsymbol{q}}, \bar{\mathbf{f}} \right) \tag{72}$$

Thus, (68) holds for arbitrary $\boldsymbol{\eta}$ and linear momentum is conserved. Substituting $\boldsymbol{c} = \mathbf{0}$ and $\boldsymbol{Q} = \exp(\epsilon \hat{\boldsymbol{\eta}})$, where $\hat{\boldsymbol{\eta}}$ is a skew-symmetric matrix, associated with the axial vector $\boldsymbol{\eta}$ so that $\hat{\boldsymbol{\eta}} \boldsymbol{a} = \boldsymbol{\eta} \times \boldsymbol{a}$ for any $\boldsymbol{a} \in \mathbb{R}^3$, we end up with

$$\mathbf{0} = \left. \frac{\mathrm{d}}{\mathrm{d}\epsilon} \right|_{\epsilon=0} \bar{\boldsymbol{\Phi}} \left( \bar{\boldsymbol{q}}^\sharp, \bar{\mathbf{f}} \right) = \eta \cdot \sum_I \boldsymbol{q}_I \times \nabla_{\boldsymbol{q}_I} \bar{\boldsymbol{\Phi}} \left( \bar{\boldsymbol{q}}, \bar{\mathbf{f}} \right) \tag{73}$$

Thus, (69) holds for arbitrary $\boldsymbol{\eta}$ and angular momentum is conserved for the semi-discrete system. The same statements are true for the reduced system, because the algebraic reformulation does not change the general characteristics of the system.



DOI: 10.1002/nme

## 4. TEMPORAL DISCRETIZATION

The semi-discrete equations of motion (47) and (50) have to be discretized in time. Consider a time interval $\mathcal{I} = [0, T] = \bigcup_{n=0}^{N-1} [t_n, t_{n+1}]$ subdivided into increments $\Delta t = t_{n+1} - t_n$ and assume the state at time $t_n$ to be known. Now, for a typical time step $t_n \to t_{n+1}$, the full discrete version of (47) reads

$$\begin{aligned} \boldsymbol{q}_{n+1} - \boldsymbol{q}_n &= \Delta t \, \boldsymbol{v}_{n+1/2} \\ \boldsymbol{M}(\boldsymbol{v}_{n+1} - \boldsymbol{v}_n) &= -\Delta t \overline{\nabla}_{\boldsymbol{q}} V(\boldsymbol{q}_n, \boldsymbol{q}_{n+1}) - \nabla_{\boldsymbol{q}} \boldsymbol{\Phi}^{\mathrm{n}}(\boldsymbol{q}_{n+1/2}) \cdot \boldsymbol{\lambda} - \boldsymbol{f}^{\mathrm{fric}}(\boldsymbol{q}_n, \boldsymbol{q}_{n+1}) \\ \boldsymbol{0} &= \boldsymbol{\Phi}^{\mathrm{n}}(\boldsymbol{q}_{n+1}) \end{aligned} \tag{74}$$

Here, $\overline{\nabla} V(\boldsymbol{q}_n, \boldsymbol{q}_{n+1})$ denotes the discrete gradient of the strain energy function [27]. The discrete version of the frictional kinematics used in $\boldsymbol{f}^{\mathrm{fric}}(\boldsymbol{q}_n, \boldsymbol{q}_{n+1}) = t_{T_\alpha} \delta \bar{\xi}^{\alpha,h}_{s,n+1/2}$ is related to the definition of the convective coordinates

$$\delta \bar{\xi}^{\alpha,h}_{s,n+1/2} = A^{\alpha\beta}_{n+1/2} \left[ \left( \delta \boldsymbol{q}^{(1)}_s - \delta \bar{\boldsymbol{q}}^{(2)}_s \right) \cdot \boldsymbol{a}_{\beta,n+1/2} + g^h_{n+1/2} \boldsymbol{n}_{n+1/2} \cdot \delta \boldsymbol{a}_\beta \right] \tag{75}$$

Note that we deal with the adjoint discrete traction $t_{T_\alpha}$ using a local evolution scheme in Appendix B. The time-discrete version of the augmented system in (50) reads

$$\begin{aligned} \boldsymbol{q}_{n+1} - \boldsymbol{q}_n &= \Delta t \, \boldsymbol{v}_{n+1/2} \\ \boldsymbol{M}(\boldsymbol{v}_{n+1} - \boldsymbol{v}_n) &= -\Delta t \overline{\nabla}_{\boldsymbol{q}} V(\boldsymbol{q}_n, \boldsymbol{q}_{n+1}) - \Delta t \nabla_{\boldsymbol{q}} \boldsymbol{\Phi}_{n+1/2} \cdot \boldsymbol{\lambda} \\ \boldsymbol{0} &= \nabla_{\mathfrak{f}} \boldsymbol{\Phi}_{n+1/2} \cdot \boldsymbol{\lambda} + \boldsymbol{f}^{\mathrm{aug}}_{n+1/2} \\ \boldsymbol{0} &= \boldsymbol{\Phi}_{n+1} \end{aligned} \tag{76}$$

where $\nabla_{\boldsymbol{q}} \boldsymbol{\Phi}_{n+1/2} = \nabla_{\boldsymbol{q}} \boldsymbol{\Phi}(\boldsymbol{q}_{n+1/2}, \mathfrak{f}_{n+1/2})$, $\nabla_{\mathfrak{f}} \boldsymbol{\Phi}_{n+1/2} = \nabla_{\mathfrak{f}} \boldsymbol{\Phi}(\boldsymbol{q}_{n+1/2}, \mathfrak{f}_{n+1/2})$, and $\boldsymbol{\Phi}_{n+1} = \boldsymbol{\Phi}(\boldsymbol{q}_{n+1}, \mathfrak{f}_{n+1})$. As already mentioned, $\boldsymbol{f}^{\mathrm{aug}}$ consists of the tractions $t_{T_\alpha}$, see (50). Accordingly, $\boldsymbol{f}^{\mathrm{aug}}_{n+1/2}$ has to be evaluated as shown in Appendix B. Following the arguments outlined in the previous section, we create a local projection matrix as follows

$$\bar{\mathfrak{P}}_{n+1/2} = -\nabla_{\boldsymbol{q}_{\mathrm{A}}} \bar{\boldsymbol{\Phi}}^{\mathrm{aug}}_{n+1/2} \left( \nabla_{\mathfrak{f}_{\mathrm{A}}} \bar{\boldsymbol{\Phi}}^{\mathrm{aug}}_{n+1/2} \right)^{-1} \tag{77}$$

and obtain for the reduced system

$$\begin{aligned} \boldsymbol{q}_{n+1} - \boldsymbol{q}_n &= \Delta t \, \boldsymbol{v}_{n+1/2} \\ \boldsymbol{M}(\boldsymbol{v}_{n+1} - \boldsymbol{v}_n) &= -\Delta t \overline{\nabla}_{\boldsymbol{q}} V(\boldsymbol{q}_n, \boldsymbol{q}_{n+1}) - \Delta t \nabla_{\boldsymbol{q}} \boldsymbol{\Phi}^n_{n+1/2} \cdot \boldsymbol{\lambda}^n - \Delta t \mathfrak{P}_{n+1/2} \boldsymbol{f}^{\mathrm{aug}}_{n+1/2} \\ \boldsymbol{0} &= \boldsymbol{\Phi}_{n+1} \end{aligned} \tag{78}$$

The second reduction step follows immediately from (60) using the discretized projection matrix in (77) evaluated at time $n + 1$

$$\bar{\mathfrak{P}}_{n+1} = -\nabla_{\boldsymbol{q}_{\mathrm{A}}} \bar{\boldsymbol{\Phi}}^{\mathrm{aug}}_{n+1} \left( \nabla_{\mathfrak{f}_{\mathrm{A}}} \bar{\boldsymbol{\Phi}}^{\mathrm{aug}}_{n+1} \right)^{-1} \tag{79}$$

The full discrete system to be solved in each Newton–Raphson iteration now reads

$$\begin{bmatrix} \boldsymbol{K}_{qq} + \boldsymbol{K}_{q\mathfrak{f}} \mathfrak{P}^T_{n+1} & \Delta t \nabla_{\boldsymbol{q}} \boldsymbol{\Phi}^n_{n+1/2} \\ \nabla_{\boldsymbol{q}}{}^T \boldsymbol{\Phi}^n_{n+1} & \boldsymbol{0} \end{bmatrix} \cdot \begin{bmatrix} \Delta \boldsymbol{q} \\ \Delta \boldsymbol{\lambda}^n \end{bmatrix} = \begin{bmatrix} \boldsymbol{R}_{q,n+1/2} - \boldsymbol{K}_{q\mathfrak{f}} \left( \nabla_{\mathfrak{f}}{}^T \bar{\boldsymbol{\Phi}}^{\mathrm{aug}}_{n+1} \right)^{-1} \boldsymbol{\Phi}^{\mathrm{aug}}_{n+1} \\ \boldsymbol{\Phi}^n_{n+1} \end{bmatrix} \tag{80}$$

where $\boldsymbol{R}_{q,n+1/2}$ consists of the residual contributions in $(78)_2$, and $\boldsymbol{K}_{qq}$ and $\boldsymbol{K}_{q\mathfrak{f}}$ denotes the consistent linearization of $\boldsymbol{R}_{q,n+1/2}$ with respect to $\boldsymbol{q}$ and $\mathfrak{f}$, respectively. In a final step, we recover the augmented coordinates by solving

$$\Delta \mathfrak{f}_A = \left( \nabla_{\mathfrak{f}_{\mathrm{A}}}{}^T \bar{\boldsymbol{\Phi}}^{\mathrm{aug}}_{n+1} \right)^{-1} \bar{\boldsymbol{\Phi}}^{\mathrm{aug}}_{n+1} + \bar{\mathfrak{P}}^T_{n+1} \Delta \boldsymbol{q}_A \tag{81}$$

for each NTS element.



DOI: 10.1002/nme

It is obvious that the linearization is extremely simplified compared with traditional schemes. Furthermore, the proposed scheme is more consistent because it ensures the exact fulfillment of the orthogonality conditions $(76)_4$ at each time node within the chosen mid-point type scheme.

### *4.1. Conservation properties*

As before, we focus on the contact contribution and begin with the verification of the conservation of linear momentum. To this end, we substitute $\delta\boldsymbol{q}_I = \boldsymbol{\eta}$, $\boldsymbol{\eta} \in \mathbb{R}^3$ into the weak form of the contact contributions

$$\begin{aligned} G^{c,h}(\boldsymbol{q}_{n+1/2},[\boldsymbol{\eta}]) = &\int\limits_{\Gamma_c^{(1)}} t_N \boldsymbol{n}_{n+1/2}\cdot(\boldsymbol{\eta}-\boldsymbol{\eta}) + \\ &t_{T_\alpha} A^{\alpha\beta}_{n+1/2}\left[(\boldsymbol{\eta}-\boldsymbol{\eta})\cdot\boldsymbol{a}_{\beta,n+1/2} + g^h_{n+1/2}\boldsymbol{n}_{n+1/2}\cdot\sum_I \hat{N}^I_{,\beta}\boldsymbol{\eta}\right]\mathrm{d}A \\ &= 0 \end{aligned} \tag{82}$$

which confirms that the constraints do not affect linear momentum conservation. Following the arguments in (66), we substitute $\delta\boldsymbol{q}_I = \boldsymbol{\eta}\times\boldsymbol{q}_{I,n+1/2}$ and obtain

$$\begin{aligned} G^{c,h}(\boldsymbol{q}_{n+1/2},[\boldsymbol{\eta}\times\boldsymbol{q}_{I,n+1/2}]) = -\boldsymbol{\eta}\cdot&\int\limits_{\Gamma_c^{(1)}} t_N\boldsymbol{n}_{n+1/2}\times g^h_{n+1/2}\boldsymbol{n}_{n+1/2} + \\ &t_{T_\alpha}A^{\alpha\beta}g^h_{n+1/2}\left[\boldsymbol{a}_{\beta,n+1/2}\times\boldsymbol{n}_{n+1/2} + \boldsymbol{n}_{n+1/2}\times\boldsymbol{a}_{\beta,n+1/2}\right]\mathrm{d}A \\ &= 0 \end{aligned} \tag{83}$$

which confirms that the constraints do not affect angular momentum conservation as well.

At last, we verify the conservation properties of the full discrete system in (76) and substitute $\delta\boldsymbol{q}_I = \boldsymbol{\eta}$

$$G^{c,h}\left(\boldsymbol{q}_{n+1/2},\boldsymbol{\eta},\mathfrak{f}_{n+1/2}\right) = \boldsymbol{\eta}\cdot\sum_I \nabla_{\boldsymbol{q}_1}\boldsymbol{\Phi}\left(\boldsymbol{q}_{n+1/2},\mathfrak{f}_{n+1/2}\right)\cdot\boldsymbol{\lambda} \tag{84}$$

whereas we obtain

$$G^{c,h}\left(\boldsymbol{q}_{n+1/2},[\boldsymbol{\eta}\times\boldsymbol{q}_{I,n+1/2}],\mathfrak{f}_{n+1/2}\right) = \boldsymbol{\eta}\cdot\sum_I \boldsymbol{q}_{I,n+1/2}\times\nabla_{\boldsymbol{q}_1}\boldsymbol{\Phi}\left(\boldsymbol{q}_{n+1/2},\mathfrak{f}_{n+1/2}\right)\cdot\boldsymbol{\lambda} \tag{85}$$

if we substitute $\delta\boldsymbol{q} = \boldsymbol{\eta}\times\boldsymbol{q}_{I,n+1/2}$. Once again frame indifference of the vector of constraints $\boldsymbol{\Phi}(\boldsymbol{q},\mathfrak{f})$ against rigid body motions is crucial for the fulfillment of the conservation laws. Proceeding along the lines of Section 3.3, we can easily verify that

$$\bar{\boldsymbol{\Phi}}\left(\bar{\boldsymbol{q}}^\sharp_{n+1/2},\bar{\mathfrak{f}}_{n+1/2}\right) = \bar{\boldsymbol{\Phi}}\left(\bar{\boldsymbol{q}}_{n+1/2},\bar{\mathfrak{f}}_{n+1/2}\right) \tag{86}$$

where $\bar{\boldsymbol{q}}^\sharp_{I,n+1/2} = \boldsymbol{c} + \boldsymbol{Q}\bar{\boldsymbol{q}}_{I,n+1/2}$. Substituting $\boldsymbol{c} = \epsilon\boldsymbol{\eta}$, $\boldsymbol{\eta}\in\mathbb{R}^3$, $\boldsymbol{Q} = \boldsymbol{I}$ yields

$$\boldsymbol{0} = \frac{\mathrm{d}}{\mathrm{d}\epsilon}\bigg|_{\epsilon=0}\bar{\boldsymbol{\Phi}}\left(\bar{\boldsymbol{q}}^\sharp_{n+1/2},\bar{\mathfrak{f}}_{n+1/2}\right) = \boldsymbol{\eta}\cdot\sum_I\nabla_{\boldsymbol{q}_1}\bar{\boldsymbol{\Phi}}\left(\bar{\boldsymbol{q}}_{n+1/2},\bar{\mathfrak{f}}_{n+1/2}\right) \tag{87}$$

Analogous to the semi-discrete system, linear momentum is algorithmically conserved. Substituting $\boldsymbol{c} = \boldsymbol{0}$ and $\boldsymbol{Q} = \exp(\epsilon\hat{\boldsymbol{\eta}})$ yields

$$\boldsymbol{0} = \frac{\mathrm{d}}{\mathrm{d}\epsilon}\bigg|_{\epsilon=0}\bar{\boldsymbol{\Phi}}\left(\bar{\boldsymbol{q}}^\sharp_{n+1/2},\bar{\mathfrak{f}}_{n+1/2}\right) = \boldsymbol{\eta}\cdot\sum_I\boldsymbol{q}_{I,n+1/2}\times\nabla_{\boldsymbol{q}_1}\bar{\boldsymbol{\Phi}}\left(\bar{\boldsymbol{q}}_{n+1/2},\bar{\mathfrak{f}}_{n+1/2}\right) \tag{88}$$

Thus, angular momentum is algorithmically conserved for the full-discrete system. Note that the last statement is also true for the reduced system, because the algebraic reformulation of the system does not change any properties of the underlying formulation.



DOI: 10.1002/nme

## 5. NUMERICAL RESULTS

In this section, we evaluate the accuracy and performance of the newly proposed method and compare the results to well-known and established methods. To solve the arising nonlinear system of equations, a Newton–Raphson solution procedure has been implemented.

### *5.1. Contact of two elements*

To evaluate the properties of the algorithms under consideration, we investigate a simple nonlinear three-dimensional example, which is constructed such that we obtain reproducible results. In particular, we consider two 3D elements, using trilinear shape functions. A compressible Neo–Hookean material is used with associated strain energy density function

$$W(\boldsymbol{C}) = \frac{\mu}{2}[\mathrm{tr}(\boldsymbol{C}) - 3] + \frac{\lambda}{2}(\ln J)^2 - \mu \ln J \tag{89}$$

where $J = \sqrt{\det(\boldsymbol{C})}$ and $\mu_l = 865.3846$, $\lambda_l = 1298.1$ are Lamé parameters corresponding to a Young's modulus of $E = 2250$ and a Poisson's ratio of $\nu = 0.3$. The reference density is given by $\rho_0 = 1000$ and the coefficient of friction $\mu = 0.5$. The initial position of the 16 nodes are given in Table I together with the initial velocity (Figure 4). Because of the initial configuration, the tangent vectors $\boldsymbol{a}_\alpha$ of the master surface are not orthonormal.

Both elements are flying free in space, that is, no boundary conditions are prescribed. First, we show results using an implicit Euler backward algorithm. Therefore, the z-position of node 8 of the upper block, which is directly in contact with the lower block, is plotted over time in Figures 5 and 6. In particular, Figure 5 shows the results for different time step sizes of the newly proposed algorithm using both reduction steps, whereas Figure 6 shows the results of the conventional direct approach. As expected, the Euler backward algorithm damps oscillations for larger time step sizes. In Figure 7, we show a comparison of the augmented system, the reduced system, and the direct approach for a

Table I. Nodal positions and initial velocity.

| Node | Position | Velocity | Node | Position | Velocity |
|---|---|---|---|---|---|
| 1 | [−0.5, −1, 2.1] | [0, 0.1, −0.04] | 1 | [−1, −1, 1] | [0 0 0] |
| 2 | [−0.5, 0, 2.1] | [0, 0.1, −0.04] | 2 | [−1.5, 1.5, 1] | [0 0 0] |
| 3 | [−0.5, −1, 1.1] | [0, 0.1, −0.04] | 3 | [−1, −1, 0] | [0 0 0] |
| 4 | [−0.5, 0, 1.1] | [0, 0.1, −0.04] | 4 | [−1.5, 1.5, 0] | [0 0 0] |
| 5 | [ 0.5, −1, 2.1] | [0, 0.1, −0.04] | 5 | [1, −1, 1] | [0 0 0] |
| 6 | [ 0.5, 0, 2.1] | [0, 0.1, −0.04] | 6 | [1.2, 1, 1] | [0 0 0] |
| 7 | [ 0.5, −1, 1.1] | [0, 0.1, −0.04] | 7 | [1, −1, 0] | [0 0 0] |
| 8 | [ 0.5, 0, 1.1] | [0, 0.1, −0.04] | 8 | [1.2, 1, 0] | [0 0 0] |

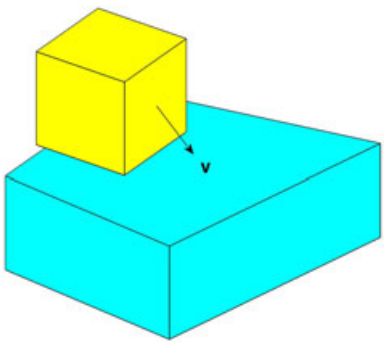


Figure 4. Reference configuration and initial velocity $\boldsymbol{v}$.



DOI: 10.1002/nme

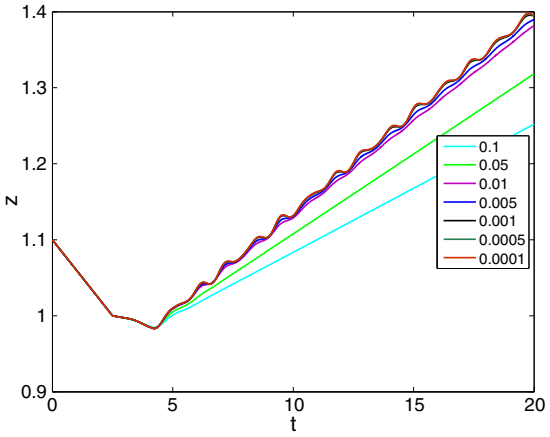


Figure 5. Augmented coordinates, z-position of node 8 plotted over time.

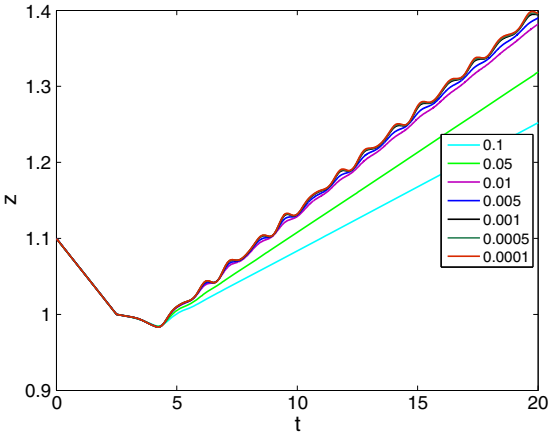


Figure 6. Direct approach, z-position of node 8 plotted over time.

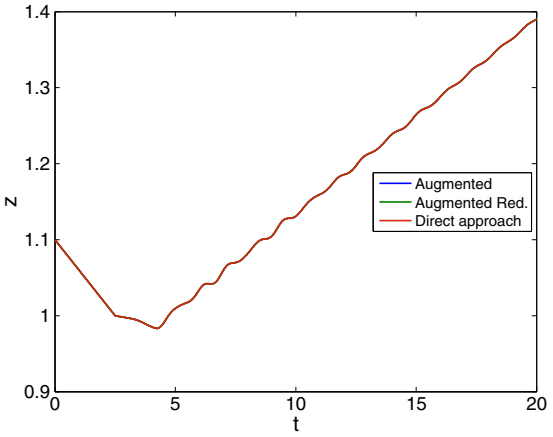


Figure 7. Comparison of the different approaches under consideration.

time step size of $\Delta t = 0.005$. The results coincide extremely well for the used implicit Euler backward algorithm. Thus, the advantages of the new approach considered here relies on the simplified structure of the contact element.



DOI: 10.1002/nme

Figure 8 shows additionally the results of the proposed new algorithm using a mid-point type evaluation, as proposed in Section 4. Using the mid-point type evaluation, we obtain even for large time

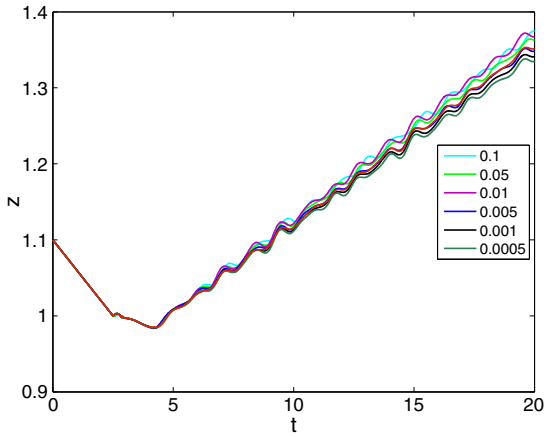


Figure 8. Augmented coordinates, mid-point type evaluation.

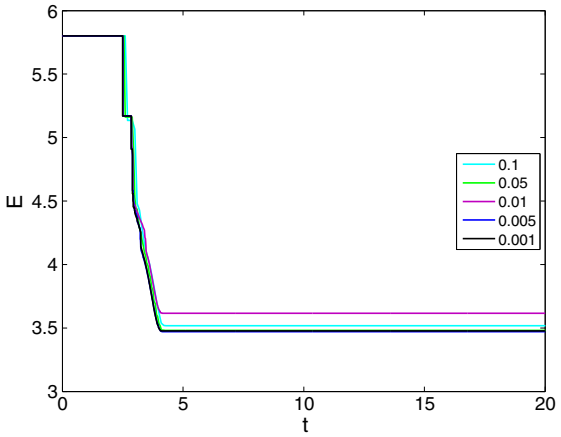


Figure 9. Total energy over time.

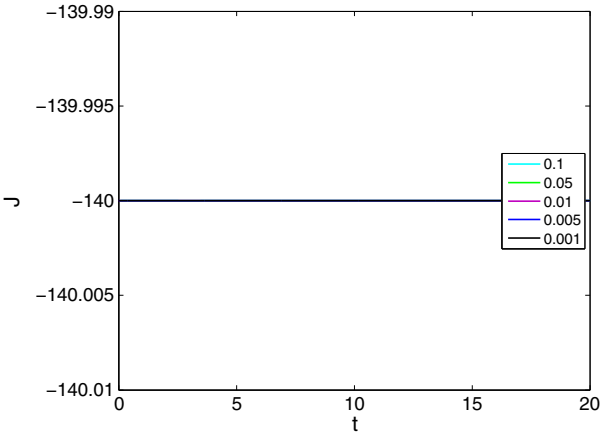


Figure 10. Total angular momentum over time.



DOI: 10.1002/nme

step sizes reliable results, for example, for $\Delta t = 0.2$, using only 100 time steps for the whole simulation. Note that Lagrange multipliers have been used to enforce the constraints in normal direction throughout all shown examples.

Finally, total energy and total angular momentum are plotted in Figures 9 and 10 for the proposed scheme using the mid-point type evaluation. As can be seen, total energy is conserved after the frictional impact. Furthermore, total angular momentum is also conserved. Although not shown here, linear momentum is also conserved algorithmically.

### *5.2. Two tori impact problem*

In this example, we consider an impact problem of two tori to demonstrate that the proposed algorithm is suitable for large systems. Initial values and the material properties have been taken from Yang and Laursen [28]. The initial configuration is displayed in Figure 11. The inner and outer

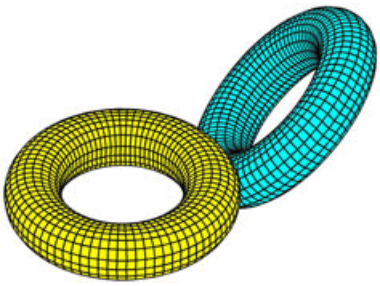

Figure 11. Initial configuration of the two tori impact problem.

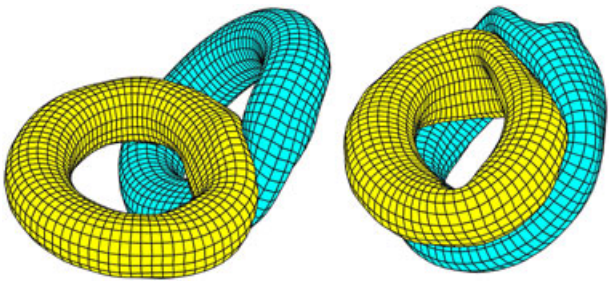

Figure 12. Deformation at time 2.5 and 5.

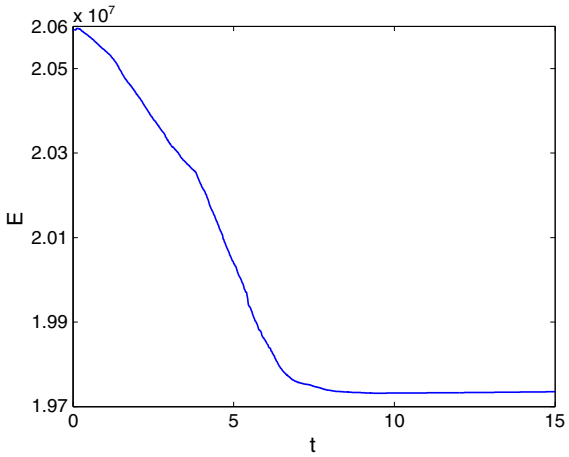


Figure 13. Total energy plotted over time.



DOI: 10.1002/nme

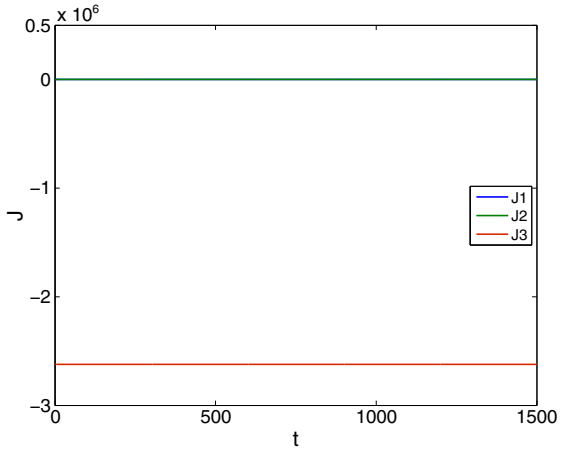


Figure 14. Components of angular momentum plotted over time.

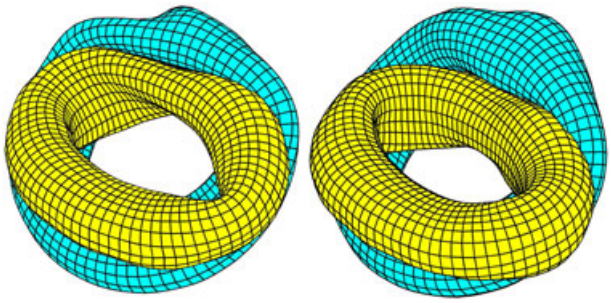

Figure 15. Comparison at $t = 5$ for $\mu = 0.1$ (left) and $\mu = 0.3$ (right).

radius of the tori are 52 and 100; the wall thickness of each hollow torus is 4.5. Both tori are subdivided into 8024 elements, using a Neo–Hookean hyperelastic material with $E = 2250$ and $\nu = 0.3$. The initial densities are $\rho = 0.1$ and the homogeneous, initial velocity of the left torus is given by $\boldsymbol{v} = [30, 0, 23]$. A time step size of 0.01 has been used throughout the whole simulation. The deformation at different time steps is shown in Figure 12.

The evolution of the total energy is shown in Figure 13, whereas the three components of angular momentum are shown in Figure 14. As expected, total energy decreases because of the frictional behavior. Because we used the proposed mid-point type evaluation of the system, angular momentum is conserved.

Finally, Figure 15 shows the deformation at $t = 5$ for different friction coefficients, using $\mu = 0.1$ and $\mu = 0.3$. The deformation changes significantly because large sliding effects are directly correlated with the friction coefficient.

## 6. CONCLUSIONS

A novel formulation for the frictional kinematics has been developed in the framework of large deformation contact. This new method rests on an augmentation technique, which substantially simplifies the underlying expressions at the cost of an enlarged global system of algebraic equations to be solved. To remedy this drawback, a size-reduction procedure has been proposed on the basis of the elimination of the Lagrange multipliers associated with the augmented coordinates. In a second step, the size of the system has been further reduced to the original size. In this connection, a new analytical representation of the projection of the convective coordinates to the configuration space has been established.



DOI: 10.1002/nme

The new approach is much more simple compared with traditional methods. As shown, the internal Newton iteration to determine the actual convective coordinates has been removed, and the residual and the tangent contributions of the contact element are significantly simplified. We have demonstrated the usability of the proposed augmentation technique for large deformation problems. Because the size-reduction of the system relies on an analytical reformulation, the underlying conservation laws are not affected. Thus, we could ensure algorithmic conservation of linear and angular momentum. This provides enhanced numerical stability of the method for large simulations.

## APPENDIX A: CONSTITUTIVE EVOLUTION EQUATIONS

Many researchers have investigated various constitutive laws used to describe the tangential tractions. We omit a further investigation and focus on a standard dry friction Coulomb law to complete the set of equations used for the numerical examples. On the basis of this specific formulation, we state that

$$\|\boldsymbol{t}_T\| \leqslant \mu\, t_N \quad \text{and} \quad \phi := \|\boldsymbol{t}_T\| - \mu\, t_N \leqslant 0 \tag{A.1}$$

The tangential displacement in the case of slip follows from $\boldsymbol{u}_T = \zeta\, \boldsymbol{t}_T$ where $\zeta$ denotes the consistency parameter, which depends on (A.1), and we can write

$$\zeta \begin{cases} = 0, & \text{if} \quad \phi < 0 \\ \geqslant 0, & \text{else if} \quad \|\boldsymbol{t}_T\| = \mu\, t_N \end{cases} \tag{A.2}$$

In analogy to plasticity, we rewrite the last statement as follows

$$\begin{aligned} &\phi \leqslant 0, \quad \zeta \geqslant 0, \quad \zeta\phi = 0 \\ &\boldsymbol{v}_T = \zeta \left( \frac{\partial}{\partial \boldsymbol{t}_T}\, \phi \right) = \zeta\, \frac{\boldsymbol{t}_T}{\|\boldsymbol{t}_T\|} \end{aligned} \tag{A.3}$$

and regularize the equation for the tangential velocity $\boldsymbol{v}_T$ $(A.3)_2$ using a penalty method

$$\boldsymbol{v}_T = \zeta\, \frac{\boldsymbol{t}_T}{\|\boldsymbol{t}_T\|} + \frac{1}{\epsilon_T}\, \dot{\boldsymbol{t}}_T \tag{A.4}$$

(Figure A.1). Note that the components in tangential direction read

$$\frac{\dot{t}_{T\alpha}}{\epsilon_T} = m_{\alpha\beta}\, \dot{\xi}^\beta - \zeta\, \frac{t_{T\alpha}}{\|\boldsymbol{t}_T\|} \tag{A.5}$$

where we have made use of $\boldsymbol{v}_T = m_{\alpha\beta}\, \dot{\xi}^\beta\, \boldsymbol{a}^\alpha$.

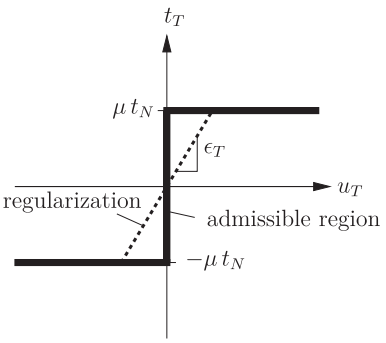


Figure A.1. Admissible region for tangential traction $t_T$ in case of Coulomb law.



DOI: 10.1002/nme

## APPENDIX B: LOCAL TIME STEPPING SCHEME FOR THE FRICTIONAL EVOLUTION EQUATIONS

Here, we apply a one-step integration scheme of the local evolution equations (A.5) following the arguments in the work of Armero and Petöcz [14]. Consequently, the approximation of the tractions can be written as follows

$$t_{T_{\alpha,n+\vartheta}} - t_{T_{\alpha,n}} = \epsilon_T \, m_{\alpha\beta_{n+\vartheta}} \left( \xi^{\beta}_{n+\vartheta} - \xi^{\beta}_{n} \right) - \epsilon_T \, \zeta \, \frac{t_{T_{\alpha,n+\vartheta}}}{\| \boldsymbol{t}_{T_{n+\vartheta}} \|} \tag{B.1}$$

where $\vartheta \in [0, 1]$ controls the corresponding time stepping scheme and should be chosen consistent with the global time stepping scheme. Taking the inequality conditions (A.3) into account, we obtain

$$\begin{aligned} \phi_{n+\vartheta} &= \| \boldsymbol{t}_{T_{n+\vartheta}} \| - \mu \, t_N \leqslant 0, \quad \zeta \geqslant 0, \quad \zeta \, \phi_{n+\vartheta} = 0 \\ t_{T_{\alpha,n+\vartheta}} &= t_{T_{\alpha,n}} + \epsilon_T \, (m_{\alpha\beta_{n+\vartheta}} \left( \xi^{\beta}_{n+\vartheta} - \xi^{\beta}_{n}) - \zeta \, \vartheta \, \frac{t_{T_{\alpha,n+\vartheta}}}{\| \boldsymbol{t}_{T_{n+\vartheta}} \|} \right) \end{aligned} \tag{B.2}$$

Note that $t_N$ is represented by a Lagrange multiplier, constant within the time step. To implement (B.2), we apply a return mapping scheme and start by considering the stick case, that is, $\zeta = 0$

$$\begin{aligned} t^{tr}_{T_{\alpha,n+\vartheta}} &= t_{T_{\alpha,n}} + \epsilon_T \, m_{\alpha\beta_{n+\vartheta}} \, (\xi^{\beta}_{n+\vartheta} - \xi^{\beta}_{n}) \\ \phi^{tr}_{n+\vartheta} &= \| \boldsymbol{t}^{tr}_{T_{n+\vartheta}} \| - \mu \, t_N \leqslant 0 \end{aligned} \tag{B.3}$$

which defines our trial state. Depending on the condition $(B.3)_2$, slip occurs, and we obtain

$$t^{tr}_{T_{\alpha,n+\vartheta}} = \epsilon_T \, \vartheta \, \zeta \, \frac{t_{T_{\alpha,n+\vartheta}}}{\| \boldsymbol{t}_{T_{n+\vartheta}} \|} + t_{T_{\alpha,n+\vartheta}} \tag{B.4}$$

by comparing $(B.2)_2$ and $(B.3)_1$. After short calculations using the relation $\boldsymbol{t}^{tr}_{T_{n+\vartheta}} / \| \boldsymbol{t}^{tr}_{T_{n+\vartheta}} \| = \boldsymbol{t}_{T_{n+\vartheta}} / \| \boldsymbol{t}_{T_{n+\vartheta}} \|$, the consistency parameter in the case of slip is determined by

$$\zeta = \frac{\phi^{tr}_{n+\vartheta}}{\vartheta \, \epsilon_T} > 0 \tag{B.5}$$

Thus, the final contribution in the case of slip reads

$$t_{T_{\alpha,n+\vartheta}} = \mu \, t_{N_{n+\vartheta}} \, \frac{t_{T_{\alpha,n+\vartheta}}}{\| \boldsymbol{t}^{tr}_{T_{n+\vartheta}} \|} \tag{B.6}$$

To summarize, the return mapping scheme can be written as follows

$$t_{T_{\alpha,n+\vartheta}} = \begin{cases} t^{tr}_{T_{\alpha,n+\vartheta}}, & \text{if } \phi^{tr}_{n+\vartheta} \leqslant 0 \\ \mu \, t_{N_{n+\vartheta}} \, \dfrac{t^{tr}_{T_{\alpha,n+\vartheta}}}{\| \boldsymbol{t}^{tr}_{T_{n+\vartheta}} \|}, & \text{else if } \phi^{tr}_{n+\vartheta} > 0 \end{cases} \tag{B.7}$$

which completes the used definition for the tractions.

ACKNOWLEDGEMENTS

Support for this research was provided by the Deutsche Forschungsgemeinschaft (DFG) under grant HE 5943/1-1 and HE 5943/3-1. This support is gratefully acknowledged.



DOI: 10.1002/nme

## REFERENCES


1. Laursen TA. *Computational Contact and Impact Mechanics*. Springer-Verlag: Berlin, Heidelberg, 2002.
2. Wriggers P. *Computational Contact Mechanics*, 2nd edition. Springer-Verlag: New York, 2006.
3. He QC, Curnier A. Anisotropic dry friction between two orthotropic surfaces undergoing large displacements. *European Journal of Mechanics - A/Solids* 1993; **12**(5):631–666.
4. Laursen TA, Oancea VG. On the constitutive modeling and finite element computation of rate-dependent frictional sliding in large deformations. *Computer Methods in Applied Mechanics and Engineering* 1997; **143**:197–227.
5. Simo JC, Hughes TJR. *Computational inelasticity*. Springer-Verlag: New York, Berlin, 1997.
6. Laursen TA, Simo JC. A continuum-based finite element formulation for the implicit solution of multibody, large deformation frictional contact problems. *International Journal for Numerical Methods in Engineering* 1993; **36**:3451–3485.
7. Konyukhov A. *Geometrically Exact Theory for Contact Interactions*, Habilitationsschrift edition. KIT: Karlsruhe, 2010.
8. Wriggers P, Simo J. A note on tangent stiffnesses for fully nonlinear contact problems. *Communications in Numerical Methods in Engineering* 1985; **1**:199–203.
9. Parisch H. A consistent tangent stiffness matrix for three-dimensional non-linear contact analysis. *International Journal for Numerical Methods in Engineering* 1989; **28**:1903–1812.
10. Betsch P, Uhlar S. Energy-momentum conserving integration of multibody dynamics. *Multibody System Dynamics* 2007; **17**(4):243–289.
11. Laursen TA, Chawla V. Design of energy conserving algorithms for frictionless dynamic contact problems. *International Journal for Numerical Methods in Engineering* 1997; **40**:863–886.
12. Chawla V, Laursen TA. Energy consistent algorithms for frictional contact problems. *International Journal for Numerical Methods in Engineering* 1998; **42**:799–827.
13. Armero F, Petöcz E. Formulation and analysis of conserving algorithms for frictionless dynamic contact/impact problems. *Computer Methods in Applied Mechanics and Engineering* 1998; **158**:269–300.
14. Armero F, Petöcz E. A new dissipative time-stepping algorithm for frictional contact problems: Formulation and analysis. *Computer Methods in Applied Mechanics and Engineering* 1999; **179**:159–178.
15. Hesch C, Betsch P. Transient 3D Domain Decomposition Problems: Frame-indifferent mortar constraints and conserving integration. *International Journal for Numerical Methods in Engineering* 2010; **82**:329–358.
16. Hesch C, Betsch P. Transient 3D contact problems – NTS method: Mixed methods and conserving integration. *Computational Mechanics* 2011; **48**:437–449.
17. McDevitt TW, Laursen TA. A mortar-finite element formulation for frictional contact problems. *International Journal for Numerical Methods in Engineering* 2000; **48**:1525–1547.
18. Hüeber S, Wohlmuth BI. A primal-dual active set strategy for non-linear multibody contact problems. *Computer Methods in Applied Mechanics and Engineering* 2005; **194**:3147–3166.
19. Hager C, Hüeber S, Wohlmuth B. A stable energy conserving approach for frictional contact problems based on quadrature formulas. *International Journal for Numerical Methods in Engineering* 2008; **73**:205–225.
20. Hesch C, Betsch P. A comparison of computational methods for large deformation contact problems of flexible bodies. *ZAMM* 2006; **86**:818–827.
21. Hesch C, Betsch P. A mortar method for energy-momentum conserving schemes in frictionless dynamic contact problems. *International Journal for Numerical Methods in Engineering* 2009; **77**:1468–1500.
22. Hesch C, Betsch P. Transient 3D contact problems – Mortar method: Mixed methods and conserving integration. *Computational Mechanics* 2011; **48**:461–475.
23. Konyukhov A, Schweizerhof K. Covariant description for frictional contact problems. *Computer Methods in Applied Mechanics and Engineering* 2005; **35**:190–213.
24. Gitterle M, Popp A, Gee W, Wall WA. Finite deformation frictional mortar contact using a semi-smooth Newton method with consistent linearization. *International Journal for Numerical Methods in Engineering* 2010; **84**:543–571.
25. Hüeber S, Stadler G, Wohlmuth BI. A primal-dual active set algorithm for three-dimensional contact problems with Coulomb friction. *SIAM Journal on Scientific Computing* 2008; **30**:572–596.
26. Tur M, Fuenmayor FJ, Wriggers P. A mortar-based frictional contact formulation for large deformations using Lagrange multipliers. *Computer Methods in Applied Mechanics and Engineering* 2009; **198**:2860–2873.
27. Betsch P, Steinmann P. Conservation Properties of a Time FE Method. Part III: Mechanical systems with holonomic constraints. *International Journal for Numerical Methods in Engineering* 2002; **53**:2271–2304.
28. Yang B, Laursen TA. A contact searching algorithm including bounding volume trees applied to finite sliding mortar formulation. *Computational Mechanics* 2008; **41**:189–205.




DOI: 10.1002/nme